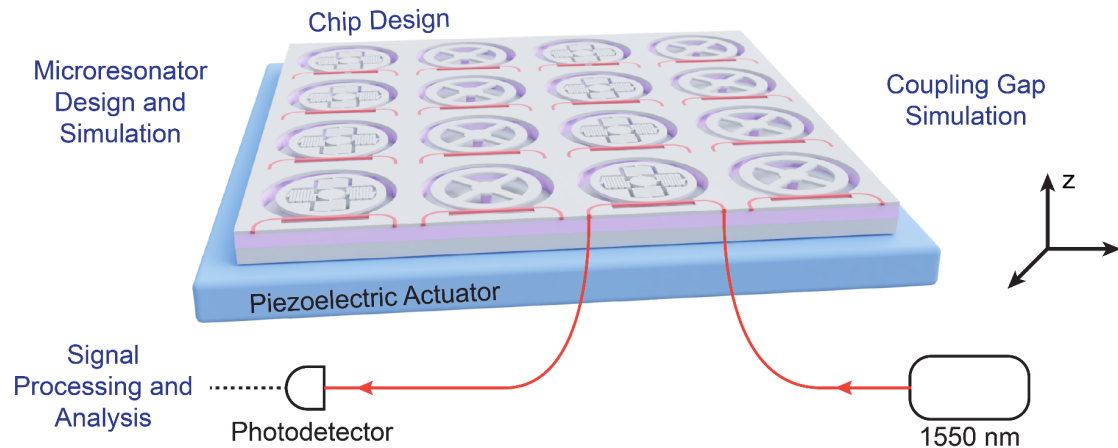


# High Throughput Testing of Coating Mechanical Loss for Advanced LIGO



Alexi Garbuz  
Bridget Meyboom  
Ruiheng Su  
Dora Yang

Project Sponsors:  
Dr. Jeff Young  
Dr. Kirsty Gardner  
Dr. Matthew Mitchell

Project 2205, ENPH 459  
Engineering Physics Project Laboratory  
The University of British Columbia  
April 8, 2022

## Executive Summary

The Laser Interferometer Gravitational Wave Observatory (LIGO) detects gravitational waves by measuring tiny distortions in space using laser interferometry. Brownian motion of molecules that make up mirror coatings are a source of noise, known as coating thermal noise (CTN), that decrease the sensitivity of LIGO detectors.

At UBC, the LIGO coating group is working to synthesize quiet thin film mirror coatings, which need to be tested and measured to estimate their CTN. To quickly explore the parameter space of different coatings (such as chemical composition, doping, and thickness), a high-throughput testing system is required.

One method of estimating CTN is to measure thin film mechanical loss, a quantity that comes from measuring the change in the time it takes for mechanical vibrations of a resonator to come to rest, before and after applying a coating. Our sponsors proposed to use disk resonators microfabricated on a 15mm x 15mm SOI chip. We proposed to use the change transmission of light through a waveguide fabricated next to each microdisk as the entire sample is vibrated by a piezoelectric actuator.

We focused on the design of the sample. We confirmed that the waveguides in our design would not oscillate at the same frequencies as the disk. To achieve the most sensitive ringdown measurements the separation between the waveguide and the microdisk should be less than 100 nm and the disk should be fabricated at about a 300 nm vertical offset from the waveguide. We also proposed new microdisk geometries with low eigenfrequencies (< 3 kHz at 500 microns). We also wrote python scripts to acquire data from an oscilloscope, analyse the noise in a measurement, filtering, and parameter extraction from data.

Based on our findings, we used python scripts to automated the CAD layout of waveguides and resonators on the sample to be used for future fabrication and testing of the whole system.

<b>Table of Contents</b>	
<b>Executive Summary</b>	<b>1</b>
<b>Table of Contents</b>	<b>2</b>
<b>List of Figures</b>	<b>4</b>
<b>List of Tables</b>	<b>6</b>
<b>Introduction</b>	<b>7</b>
Our Sponsors	7
Background	7
Project Objectives	8
Project Scope	8
<b>Discussion</b>	<b>9</b>
Theory and Fundamentals	9
Design, Method and Approach	11
Mechanistic Overview of System	11
Microdisk Design	11
Evanescence Coupling	16
Waveguide design	17
Evanescence coupling displacement sensing	18
Chip Design	21
Signal Processing	23
Data acquisition	24
Signal-to-noise ratio measurement	24
Envelope extraction by lock-in demodulation	26
Envelope extraction by analytic signal	26
<b>Conclusion</b>	<b>28</b>
<b>Recommendations</b>	<b>29</b>
Microdisks:	29
Next steps:	30
Waveguide	30
Next steps	30
Evanescence coupling	31
Next steps	31
Chip Design	31
Next steps	31
Signal Processing	31
<b>Deliverables</b>	<b>32</b>
<b>Works Cited</b>	<b>33</b>

<b>Appendices</b>	<b>35</b>
Appendix A: Measuring mechanical loss using a resonator	35
Appendix B: Original microdisk design optimization	36
Appendix C: Hole microdisk design	38
Appendix D: Finalised hole microdisk design parameters	41
Appendix E: Meander arms microdisk design	43
Appendix F: Calculating wavelength of an acoustic wave in silicon	44
Appendix G: Optics and evanescent waves	45
Appendix H: Waveguide Design	46
Appendix I: Lumerical Coupling Simulations	50
Appendix J: Instrument specifications	57
Appendix K: Power spectral density is a measure of system noise	58
Appendix L: Amplitude demodulation using lock-in amplifier	60
Appendix M: Library of literature resources:	61

## List of Figures

<b>Figure Number</b>	<b>Title</b>	<b>Page Number</b>
1	SEM image of spoked microdisk design developed by UBC LIGO group	8
2	Optical Schematic of LIGO's gravitational wave detector	9
3	LIGO noise sources, strain amplitude plotted as a function of frequency	10
4	High-throughput evanescent coupling system	11
5	Two mechanical mode shapes of a microdisk resonator	12
6	Microdisk etching process	13
7	Schematic of spoked microdisk designs with annotations of key parameters	14
8	New proposed disk designs (hole and meander)	15
9	Cross-section of microdisk and PML used in Q-factor simulations	16
10	Silicon waveguide exposed by HF etching	17
11	Plot of waveguide eigenfrequency as a function of length	18
12	Lumerical model implemented for coupling gap simulations	19
13	Plot of transmission as a function of microdisk and waveguide coupling gap	20
14	Plot of transmission as a function of vertical displacement between microdisk and waveguide	20
15	Microdisk, waveguide and grating coupler cell	21
16	Proposed chip design containing updated microdisks and evanescent coupling components	22
17	Schematic of signal processing setup	23
18	Photodetector signal and corresponding PSD	25
19	Schematic overview of ringdown extraction via analytic signal	26
20	Distribution of best fit ringdown times with varying noise level and initial excitation for computer generated data	27
21	Spoked microdisk designs with annotations of key parameters	29
22	Hole microdisk design	29
23	Sponsor's spoked microdisk design	36

24	Plot of eigenfrequency vs disk radius for spoked design	36
25	Plots of eigenfrequency vs mid_arc_frac for spoked disks of various radii	37
26	Potential new hole cutout pattern	38
27	Comparison of eigenfrequencies for multiple hole designs	30
28	Final hole design	40
29	Final hole design	41
30	Variations of the meander disk design	43
31	Inspiration behind the meander disk design	43
32	Schematic demonstrating evanescent coupling between two mediums	45
33	Models that were considered for waveguide eigenfrequency simulations	46
34	Waveguide from COMSOL simulation with a swept mesh	47
35	Mesh-eigenfrequency convergence plots	47
36	Plot of waveguide eigenfrequency as a function of length	48
37	Plot of waveguide eigenfrequency as a function of width	48
38	Waveguide mode shapes generated by COMSOL	49
39	Lumerical model implemented for coupling gap simulations	50
40	Comparison of light coupling between two different simulation regions	51
41	Plot of a parameter sweep that measured the power of light versus mesh accuracy	54
42	Plot of the transmission through a waveguide as a function of the coupling gap	54
43	Plots of the transmission through a waveguide as a function of coupling gap	54
44	Plots of relative light power as a function of distance from the centre of the waveguide	55
45	Plot of the transmission of light through the waveguide as a function of the coupling gap	56
46	Transmission of light through the waveguide as a function of vertical displacement between the waveguide and a 10 $\mu\text{m}$ microdisk	57
47	Demonstration of real time envelope demodulation	61

## List of Tables

<b>Table Number</b>	<b>Title</b>	<b>Page Number</b>
1	Recommendation on parameters for spoked microdisk design	15
2	Recommendation on parameters for spoked microdisk design	29
3	Waveguide recommendations	30
4	Evanescence coupling recommendations	31
5	Hole design parameter recommendations	41
6	Waveguide parametric sweep parameters	46
7	Calculated slopes of transmission vs coupling graphs for various disk radii.	55

## Introduction

### Our Sponsors

Our sponsors for this project are Dr. Kirsty Gardner, Dr. Matthew Mitchell, and Dr. Jeff Young of the UBC's Stewart Blusson Quantum Matter Institute. They are part of a larger UBC LIGO Scientific Collaboration, and are working to develop low noise, highly reflective thin film materials for LIGO gravitational wave detectors. The UBC LIGO team can be broken down into three subteams: characterization of coating noise, theory and modelling, and coating growth and synthesis. Our sponsors are focused on characterising noise in the thin films by measuring their mechanical loss. In order to test a large range of thin film parameters, a testing setup that is high throughput and provides repeatable results is required.

### Background

There are main methods described in literature for measuring thin film mechanical loss. We will focus our discussion into two streams: displacement sensing and resonators.

At a higher level, we can quantify loss in a thin film by coating a resonator with it, driving it into oscillation, and then allowing those vibrations to dampen with time. Measuring the disk's position over time will give us a decaying sinusoidal signal, which can be used to extract a value for the loss from the thin film. For a more detailed discussion of this measurement method, see Appendix A.

Our sponsors currently use a method called Laser Doppler Vibrometry (LDV) to do this, but are limited by the manual control of the system. For an explanation of LDV, see [the Wikipedia article titled "Laser Doppler vibrometer"](#). We explored alternative displacement sensing options and ultimately decided to pursue a technique based on evanescent coupling of light.

We will now shift our attention to the resonators themselves. Literature relating to this topic explores many different resonator geometries, the most common being cantilevers and disks. For papers on resonator design, see our library in Appendix J. Our sponsor's novel approach to resonators uses disks that are on the micrometre scale (microdisks), shown in Figure 1 below, compared to centimetre-scale disks used in previous LIGO loss studies (Granata et al., 2020). Smaller resonators increase testing throughput because hundreds of microdisks can be microfabricated on a single sample. This allows hundreds of measurements for a particular thin film in a single sample, instead of one measurement per sample. Furthermore, the micrometre scale allows our sponsors to test many different resonator geometries at once to improve the testing setup since it is relatively easy to fabricate hundreds of different microdisks on one chip. An image of our sponsor's current microresonator design is shown below.

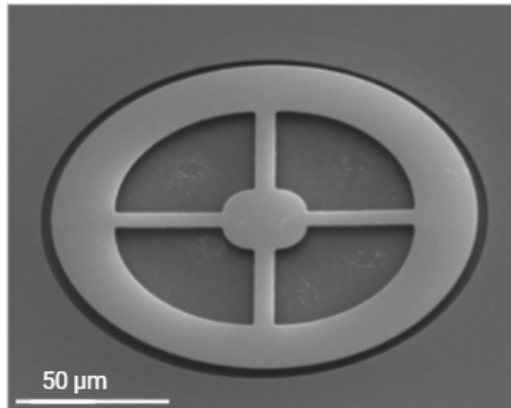


Figure 1: Top-down SEM image of the current microdisk design used by UBC sponsors.

The design in Figure 1 uses four spokes to anchor the middle of the disk to the outer ring. The darker grey regions between the spokes represent cutouts in the disk. A pedestal beneath the centre of the disk attaches it to a larger substrate. Our sponsors are looking to decrease the eigenfrequency (or natural frequency) of their microdisks from 60 kHz to between 100 Hz and 1 kHz.

## Project Objectives

Our project objectives can be summarised with one main goal: improving the sponsor's testing system to allow for more high throughput measurements of mechanical loss in thin film coatings. The key objectives were:

1. Create new microdisk geometries with eigenfrequencies between 100 Hz and 1 kHz.
2. Determine the system parameters that will produce the most sensitive evanescent coupling displacement measurements.
3. Implement a signal processing system that can extract thin film coating noise.
4. Integrate the resonator and displacement sensing findings into a final chip design for our sponsors.

## Project Scope

For the microresonator geometries, we did not explore any options that were not inherently microdisks (for example, cantilevers). We focused on the microdisk structure, and tested creative cutout designs we could employ to lower their eigenfrequencies.

For the optical probing strategy, we researched several potential methods to use, however we decided to pursue evanescent coupling for our system. The important parameters we explored for evanescent coupling (which we will describe in greater detail in the *Design Method* section) included how we would couple light onto the chip, and identifying the optimal conditions to provide the greatest sensitivity in measuring microdisk displacement using Lumerical and COMSOL simulations.

As part of the optical probing strategy, we constructed a physical setup that produced and measured modulated laser light. The setup provides a way to directly estimate the signal-to-noise ratio of the measurement technique, as a function of laser power and expected intensity modulation due to evanescent coupling. This setup also provided grounds for us to develop a suite of data acquisition and analysis programs to accelerate testing measurements in the future.

## Discussion

### Theory and Fundamentals

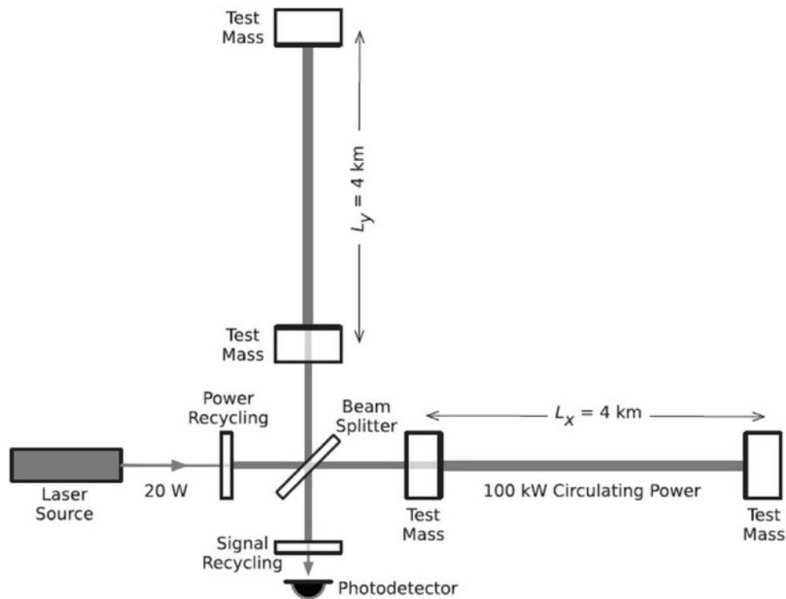


*Figure 2: Schematic of LIGO's interferometer. The laser produces a coherent beam of light that passes through a beam splitter into two beams that each travel along an interferometer arm.*

*The split beams resonate in the cavity formed by the two test masses and are eventually recombined at the beam splitter. The signal of the combined beam is measured at the photodetector.*

LIGO uses interferometry to detect distortions in spacetime on the scale of  $10^{-19}$  metres caused by gravitational waves. For details about interferometry and LIGO's detectors see [the Wikipedia article titled "LIGO"](#). One key component of the detector is the mirror coating placed on the test masses (Figure 2) of the interferometer arms. The test masses are highly reflective and form a resonant cavity for the laser light to reinforce the strength of the detection signal. Since the system needs to detect such small-scale changes in space, the system noise must be minimised. The sources that contribute to LIGO's loss of sensitivity can be seen in Figure 3. To improve the sensitivity of the next generation LIGO detectors, researchers must be able to identify "quiet" thin film coatings, through synthesis and testing.

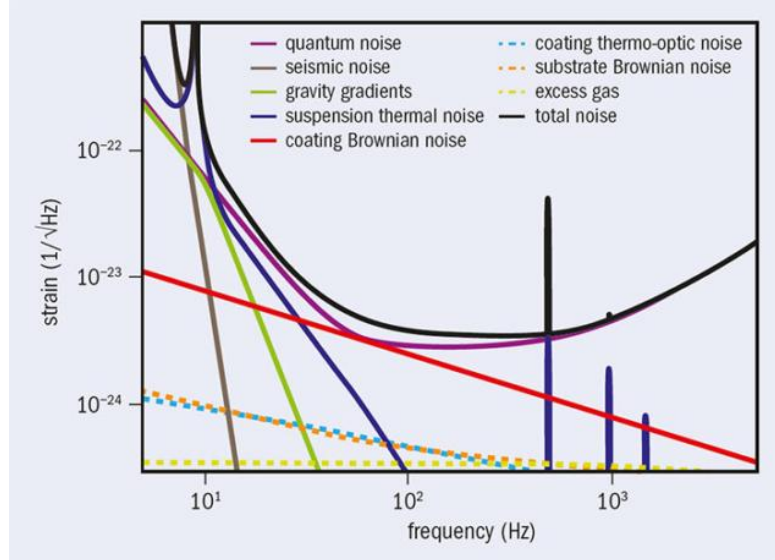


*Figure 3: Strain noise amplitude spectrum of a LIGO detector. Between 100 to 1000 Hz, coating brownian noise is a dominant noise source. Reproduced from cerncourier.com.*

Mechanical resonators play an important role in estimating coating thermal noise. Mechanical resonators are mechanical systems that have vibrational modes (or eigenmodes), where all parts of the system vibrate at the same frequency (eigenfrequency). Examples of mechanical resonators include cantilever beams, membranes, and disks suspended on pedestals.

The fluctuation dissipation theorem directly relates coating thermal noise to the coating mechanical loss - a quantity that can be extracted using a combination of simulation and by measuring the difference in ringdown time between mechanical resonator coated with the optical coating and without the optical coating when the resonator is driven at a particular eigenfrequency. We refer readers to the references (Granata et al., 2020) and (Li et al., 2014) for the full details.

## Design, Method and Approach

### Mechanistic Overview of System

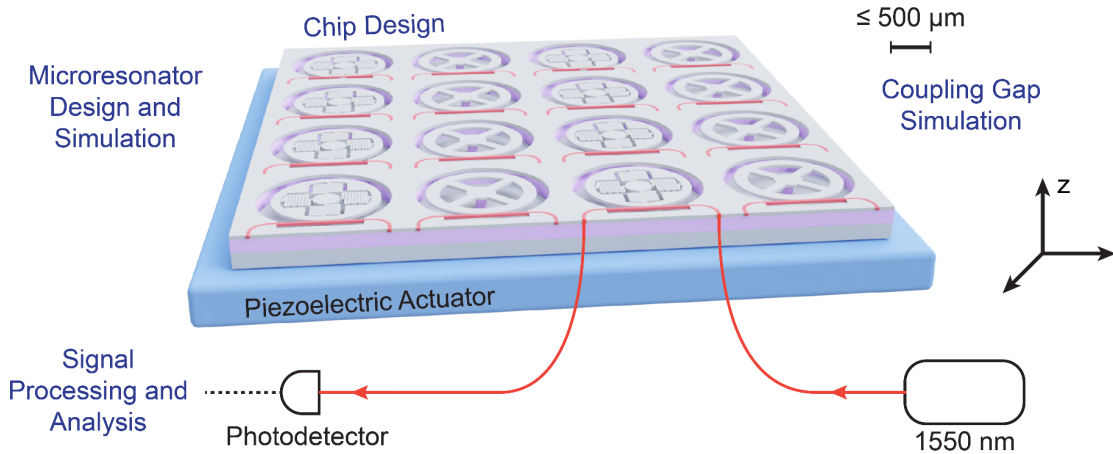


Figure 4: High-level overview of the system components (indicated in blue). The scale bar on the upper right corner indicates that Each microdisks are expected to have a radius  $\leq 500 \mu\text{m}$ .

The core of our system consists of the light source, photodetector, and a **15mm x 15mm SOI chip** that has an array of microfabricated microdisks, each paired with a waveguide grating couplers. The microdisks will oscillate in the z-direction at their natural frequency by applying an AC voltage to a piezoelectric actuator (Figure 4, illustrated in blue). The AC voltage is then removed, and the oscillation is allowed to decay.

Light is coupled in and out of each waveguide using the grating couplers. As the microdisk comes to a rest, and the action of ringing down produces an oscillating signal with our evanescent coupling method. These steps are repeated for every microdisk on the chip. The resulting signals are measured and analysed to determine the ringdown time of each disk.

### Microdisk Design

Microdisks are devices with both mechanical and optical properties. For our project, we are interested in the mechanical properties of a microdisk, specifically the natural frequency that it vibrates at (also referred to as eigenfrequency). An *eigenmode* is the shape that the disk will take when it is vibrating at its eigenfrequency ("Eigenfrequency Analysis", 2018). Each microdisk has several eigenfrequencies, each with a corresponding eigenmode. The figure below shows an example of two distinct mode shapes for a given microdisk. These are shapes the disk would take on when vibrating at two distinct eigenfrequencies.

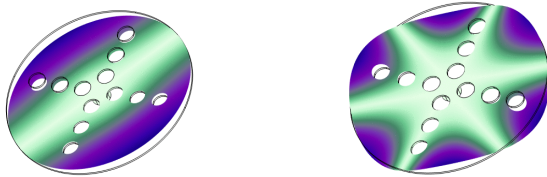


*Figure 5: On the left is a microdisk in its 1st eigenmode (resonating at its lowest eigenfrequency); on the right is the same disk in its 7th eigenmode (vibrating at its 7th lowest eigenfrequency).*

Driving these microdisks to vibrate at their eigenfrequencies is what we refer to as driving them into resonance. As shown in Theory and Fundamentals, coating thermal noise dominates in LIGO's noise spectrum between 100-1000 Hz. Thus, when we are testing the performance of thin films we want to be testing their mechanical losses at a frequency as close to 100 Hz as possible. This is why we want to create microdisk structures that have eigenfrequencies close to that range. We discussed previously how the current microdisks in use by our sponsors have an eigenfrequency of about 60 kHz in vacuum, so our goal is to minimise that eigenfrequency as much as possible.

We mentioned that each microdisk has several eigenmodes; For our design and testing we focused on the first eigenmode as this corresponds to the lowest eigenfrequency, assuming that in a vacuum, the lowest mode of the microdisks will not be significantly damped out. But if we are unable to do so, the eigenfrequency of the disks will be significantly higher due to having to measure a higher eigenmode.

In order to come up with ideas for microdisk designs, we used the following equation to guide our intuition:  $f = \frac{1}{2\pi} \sqrt{\frac{k}{m_{eff}}}$  (Sun et al.) Here,  $f$  is the frequency of a mechanical oscillator,  $k$  is the spring constant and  $m_{eff}$  is the effective mass. The key takeaway from this equation is that we will want to find a balance between decreasing stiffness ( $k$ ) and increasing mass ( $m_{eff}$ ). In general, as we saw by doing simulations, decreasing the mass in strategic locations will cause a decrease in stiffness, but then the decrease in mass consequently has a negative effect on the value we are trying to optimise. Thus, we required rigorous simulating and testing to see how each design would perform by trading off between mass and stiffness.

There were also several constraints we had to keep in mind while designing the new disks, the first one being fabrication constraints. If the radius of the disk was too large, it would be prone to breaking, thus we had an upper limit on the size of the radius which we defined with our sponsors to be 500  $\mu\text{m}$ . This number was mostly based on what the sponsors thought would be possible to fabricate. The plan was therefore to do all of our simulations assuming we could use this radius, and then our sponsors would perform a number of tests and sweeps of the microdisk radius in-lab to see the true maximum size we could fabricate without mechanical

failures. As we will discuss in the *Recommendations* section, determining this maximum disk radius is still being worked on and will be important for implementing the new designs.

Next, we had to consider etching rate while developing designs. In brief, to fabricate the microdisks, Hydrogen Fluoride (HF) is used to etch away the silicon-dioxide layer underneath the disk where we want it to be undercut. However, if we are not careful with our placement of cutouts in the disk, it is possible that within the time needed to etch away the silicon-dioxide to create the undercuts, the HF could also etch away significant parts of the pedestal and render it unstable. Figure 6 a) shows the silicon microdisk in blue attached to its silicon dioxide pedestal in green. The undercut regions illustrate where the silicon dioxide is to be etched away. The chemical HF will enter from the edges of the radius of the microdisk, but also enter through any cutouts and etch out radially from those holes (Figure 6 b)). When designing new disks, we had to ensure that not too much of the pedestal would get etched away. We could check this using calculations of how long it would take to etch the largest undercut and compare it to how much of the pedestal would (if at all) get etched away in that time from HF leaking in through the cutouts above.

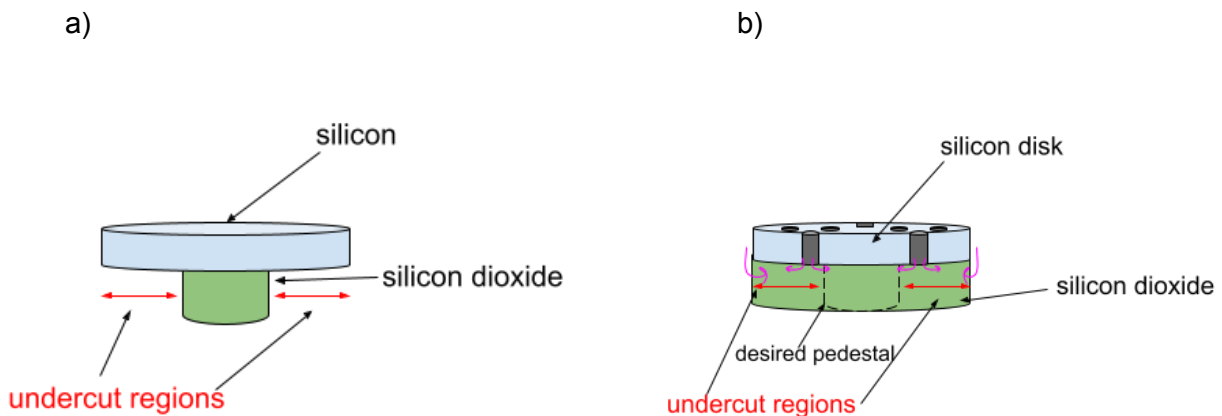


*Figure 6: a) Microdisk with pedestal, highlighting regions to be undercut (etched away) using HF. b) Grey cylinders represent holes/cutouts in the microdisk, pink arrows represent HF solution and how it will etch away the silicon dioxide as it comes in through the edge of the disk and through holes/cutouts in the disk.*

The next constraint to keep in mind has to do with mechanical stability. Different structures that are less mechanically stable will likely collapse once they are fabricated (due to uneven distribution of weight, not enough support from pedestal, etc.) This consideration is something that is harder to predict and account for in creating new designs, and can only really be tested by fabricating the structure in-lab and seeing if it collapses or not.

The last constraint we will consider is Q-Factor which is  $2\pi$  times the ratio of energy stored, to energy dissipated per oscillation cycle of a resonator (Paschotta). In the context of our project, Q-Factor is one component contributing to how quickly the oscillations of the microdisks will

dampen. A higher Q-Factor is preferred; this means less energy is being dissipated per oscillation and we will get a longer decay curve representing the microdisks ringing down. Having this longer curve will make signal processing, feature extraction and fitting much easier. Because of this it will be easier to calculate the associated mechanical loss if we have a higher Q-Factor for our design. We can measure the Q-Factor of a microdisk design using our simulation platform, which we will describe in more detail further below. Note that we are not trying to optimise Q-Factor with our new designs, rather we want to ensure that our designs do not significantly *lower* the Q-Factor compared to the microdisks the sponsors currently use.

In order to produce new microdisk structures with lower eigenfrequencies, we designed them in COMSOL Multiphysics (a simulating software) and performed rigorous simulations to test how different designs affected the eigenfrequency.

Our first task involved taking the current microdisk design the sponsors use and optimising its parameters to lower the eigenfrequency. The main parameters we varied are labelled on Figure 7 below.

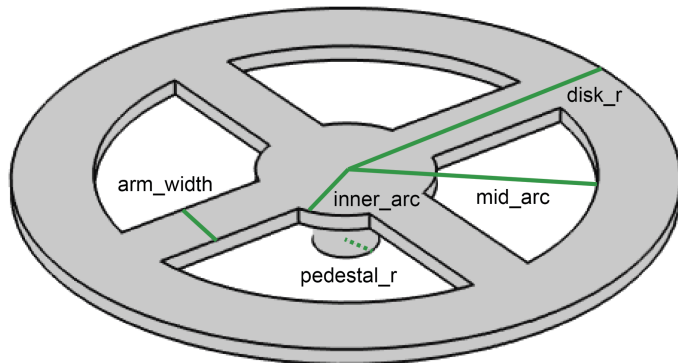


*Figure 7: Sponsor's current microdisk design labelled with parameters we varied in simulation.*

For a detailed discussion of our tests and results see Appendix B. A summary of our recommended parameter values obtained from testing, contrasted with the current parameters used by our sponsors is shown in the table below. It is important to note that by specifying to “Minimise” a feature, this will involve our sponsors performing in-lab tests to determine how small the feature can be whilst maintaining mechanical stability.

*Table 1: Table contrasting the parameter values of the microdisk the sponsors currently use vs. our recommended values based on simulation results.*

Parameter	Current Value	Recommendation
disk_r:	80 $\mu\text{m}$	Maximize (500um)
mid_arc_frac:	0.6	Tune to 0.7 - 0.8
inner_arc_frac:	0.25*disk_r	Minimize
pedestal_r:	0.25*disk_r	Minimize
arm_width:	0.05*disk_r	Minimize

Along with the improved original design, we also created two new microdisk cutout patterns. The first one involved having many smaller hole cutouts rather than the four quadrants used in the original design. For a detailed look at this design and results see Appendices C and D. With this new design we were able to reduce the simulated eigenfrequency to 3.11 kHz in vacuum.

Our second proposed design replaced the straight arms of the original microdisk by meandering arms. Our design considerations are shown in Appendix E. Due to time constraints, we did not fully explore the capabilities of this design.

For the full list of simulations performed, see this [spreadsheet](#), and for corresponding raw data, see this [folder](#).

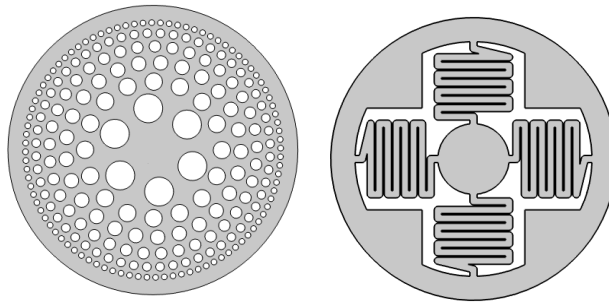


*Figure 8: Our two new proposed microdisk designs. On the left is the finalised hole design, on the right is the finalised meander design.*

As aforementioned, it is important to ensure the Q-Factor does not decrease with these new designs. We suspect that the size of the innermost holes in the design with many circular holes may affect Q-Factor. There is a built-in functionality in COMSOL that allows us to calculate Q-Factor while we do our eigenfrequency simulations. However, additional structure needs to be

added to the simulation design to mimic the entire system rather than having the microdisk be completely independent; in reality, we will have the microdisk attached through the pedestal to a much larger silicon substrate. For simulation purposes, we will add the substrate structure into the design, but since it is so much larger than the disk, in order to speed up simulation time rather than having an enormous substrate we incorporated a Perfectly Matched Layer (PML) on the outside of the substrate layer. The PML layer acts to fully absorb any of the acoustical waves being generated from the microdisk vibrations coming in through the pedestal and travelling through the substrate to where they meet the PML.

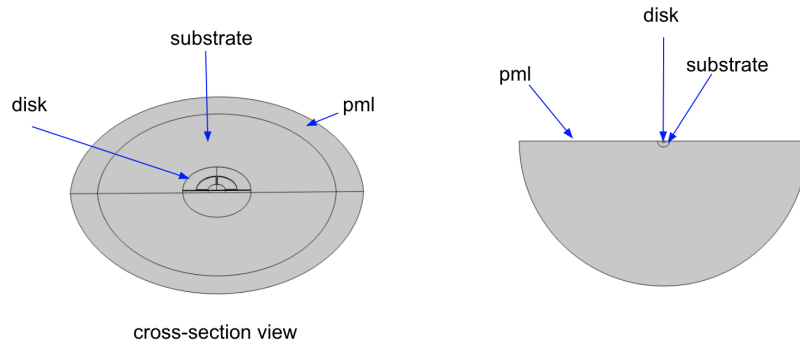


*Figure 9: The left image shows a cross-sectional view of the layering involved to do Q-factor simulations. The image on the right shows a side-on view of the structure but with a much larger PML than the left image.*

In general, the PML thickness should be around half of the wavelength of the wave we expect to travel through the substrate. For our purposes, this meant finding the lowest microdisk eigenfrequency we would expect (which depends on the design of the microdisk), and using that frequency to calculate the wavelength (see Appendix F for how to calculate the wavelength). Work still needs to be done to find an optimal PML and substrate structure to allow for robust and accurate Q-factor measurements, which we will describe more in our *Recommendations* section.

Our microdisk design has mostly centred around our simulation data in COMSOL. The next step would be to fabricate these structures and test their performance in-lab, which we describe in our *Recommendations* section later in the report.

### Evanescence Coupling

Evanescence waves are a type of electromagnetic wave that arise during total internal reflection because light cannot be discontinuous at a boundary between two different media. They do not propagate, instead their energy stays confined near the boundary and decays exponentially with distance. Evanescence coupling occurs when an evanescent wave encounters a new medium boundary before it decays fully, and generates a propagating light wave in the new medium. For more details about optics and evanescent waves, refer to Appendix G.

## Waveguide design

Waveguides are structures that guide electromagnetic waves by restricting the transmission of power to one direction. They are made of dielectric materials with high indices of refraction with an external cladding made of a lower index material so light propagates through by total internal reflection with very low loss.

We will use rectangular silicon (Si) waveguides to bring light near the vibrating microdisks and make our evanescent coupling displacement measurements. They will be fabricated onto a silica ( $\text{SiO}_2$ ) layer, by photolithography, which can be etched out to leave a portion of the waveguide exposed on all sides. The exposed waveguide allows for more evanescent waves to be generated in the vicinity of the microdisk, compared to if there was no additional etching.

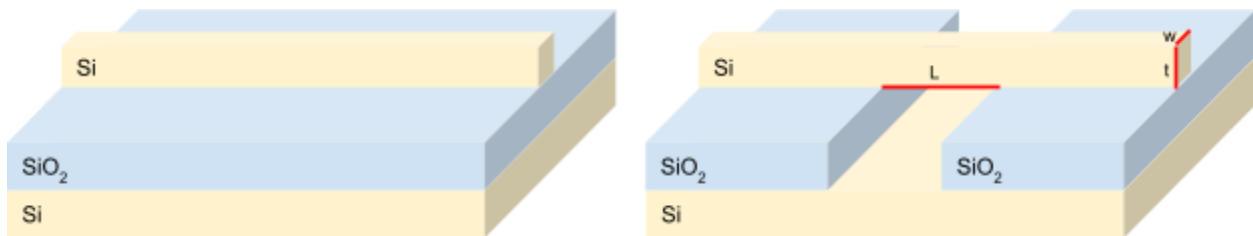


Figure 10: The silicon waveguide will be fabricated onto a silicon dioxide layer (left). The portion of the waveguide that passes near the microdisk will be exposed by etching away the silicon dioxide layer beneath it (right).

For our design, we focused on the length (L), width (w) and thickness (t) of the exposed waveguide as indicated in Figure 10. The waveguide and microdisk are both going to be fabricated out of silicon on top of the silicon dioxide layer. The thickness of the waveguide is fixed at 500 nm, the same as the microdisk.

The dimensions of the waveguide are critical for determining modes of light the waveguide carries. Single mode waveguides are typically used for scientific applications and are more desirable for our application because they limit signal distortion and loss, which is essential for making sensitive displacement measurements. To achieve this our sponsors recommended that we test waveguides with widths between 140 nm - 180 nm. Additionally, the suspended part of the waveguide must be mechanically stable. Based on previous fabrication experiences of our sponsors we limited the length of the waveguide to 200  $\mu\text{m}$ .

The key mechanism for our displacement measurements is the amount of evanescent coupling between the disk and the waveguide. Since we want to measure the ringdown of the disk we had to make sure only the disk was vibrating during measurements. To do this, we used COMSOL simulations to determine if the mechanical resonant frequencies of the waveguide would overlap with those of our microdisk designs. Refer to Appendix H for the implementation details of the simulation.

In our simulations, we varied the length of the waveguide. Since the lengths we simulated were approximately 1000 times greater than the width and thickness of the waveguide we could use the eigenfrequency equation for slender beams:

$$f \propto \frac{1}{2\pi L^2} \sqrt{\frac{k}{m}}$$

Where k is the material bending stiffness, m is the effective mass and L is the length of the waveguide. Based on this equation we expected that eigenfrequency would decrease as length is increased. We also expected that changing the width of the waveguide would not significantly change its eigenfrequency.

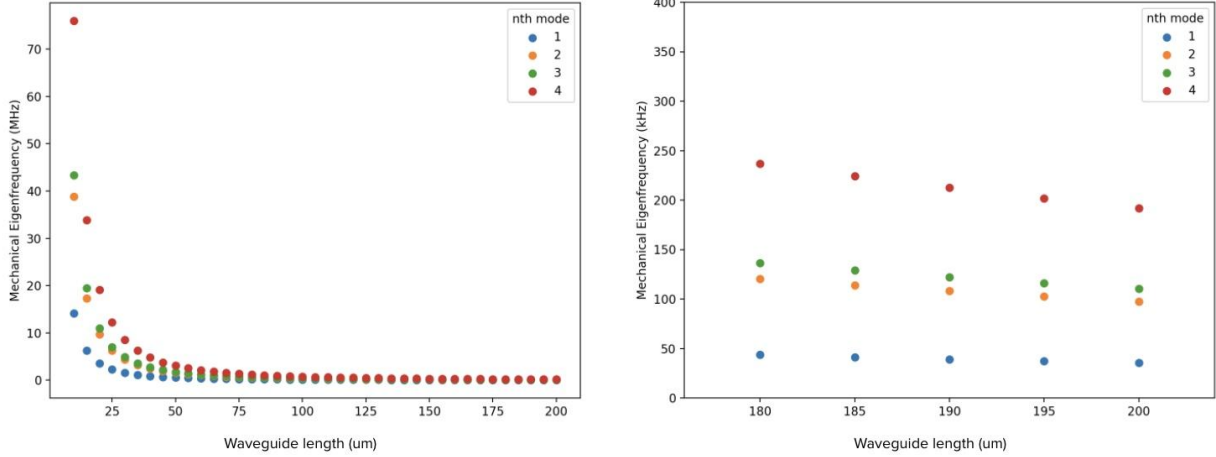


*Figure 11: On the left, eigenfrequency of first four eigenmodes of a fixed width (160 nm) waveguide as a function of length (10 μm - 200 μm). On the right, eigenfrequencies at the upper length limit (180 μm - 200 μm).*

The data in Figure 11 demonstrates that eigenfrequency of the waveguide is inversely proportional to its length, as expected. In our design, longer waveguides are ideal because that increases the length of the exposed evanescent waves that can couple into the microdisk. Looking at the upper range of lengths in the right plot of Figure 11 we see that the lowest eigenfrequencies measured are between 25 kHz - 50 kHz. This is well above the microdisk eigenfrequency range of 100 Hz - 1 kHz. From this analysis we concluded that any waveguide length we choose would not result in eigenfrequencies that overlap with the eigenfrequencies of the disks and thus our ringdown measurements will solely be dependent on the displacement of the disks.

#### Evanescence coupling displacement sensing

Our system must measure the position of the coated microdisks as they are ringing down. The amplitude of the disk's oscillations will depend on the force of the mechanical vibration driver and based on the current LDV measurements, the expected amplitude is between 100 pm and 500 pm.

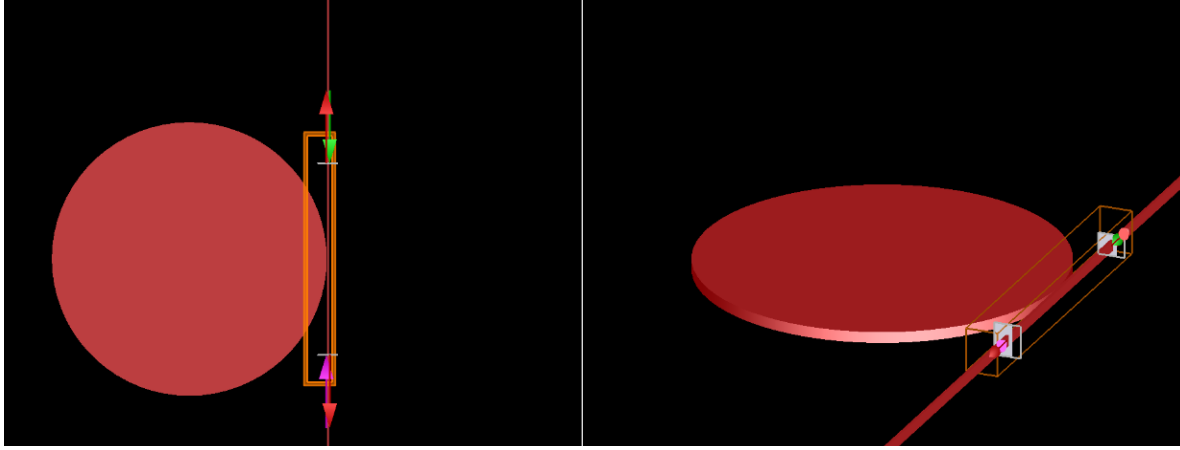


*Figure 12: Lumerical model to simulate coupling between a silicon microdisk and a silicon waveguide. The orange box defines the simulation region, and input (pink) and output (green) ports inject and monitor light in the simulation.*

Light can evanescently couple from the waveguide into the microdisk and the amount of light that couples into the disk will depend on the magnitude of the evanescent wave when it meets the disk's boundary. So, if the disk is close to the waveguide more light is coupled into the disk and less light is transmitted through the waveguide. Thus we can obtain a relative measurement of the disk's position by measuring the transmission of light through a waveguide that passes near the vibrating microdisk.

A sensitive measurement system requires a large change in transmission for small changes in displacement. We considered the following factors when optimising our design: the mode of light travelling through the waveguide, the coupling gap between the waveguide and the microdisk and the effect of vertical displacements. To determine these we used Lumerical's Finite Difference Time Domain (FDTD) solver suite to simulate the behaviour of light as it travels through a waveguide past a microdisk. The following discussion will highlight the key findings from the simulations, please refer to Appendix I for full documentation and implementation.

Modes describe how light propagates through a waveguide based on its boundary conditions. For our design we considered transverse electric (TE) and transverse magnetic modes (TM). Through simulations, we computed power as a function of distance from the light source. We found that the power distribution over space changed for TE modes depending on the wavelength of light and waveguide dimensions and was invariant for TM modes. We also saw that using a TM light source yielded larger changes in transmission for the same change in distance than TE modes.

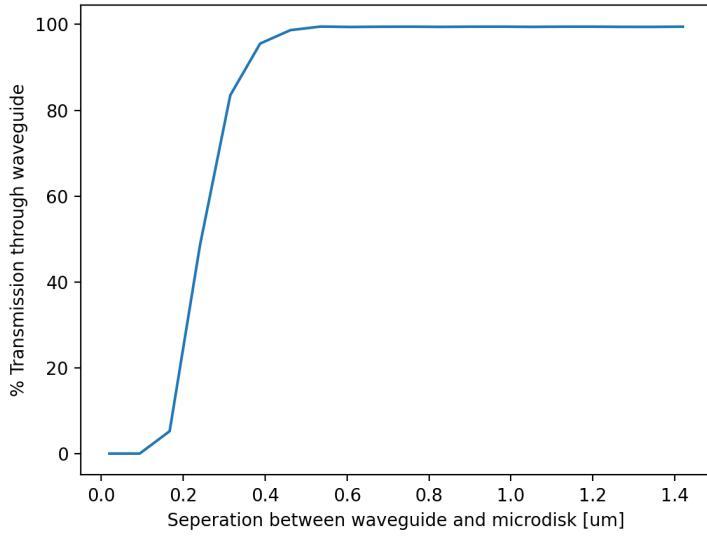


*Figure 13: Plot of the transmission of light through the waveguide as a function of the coupling gap between the 500  $\mu\text{m}$  radius disk and the waveguide. Coupling began at a separation of 500 nm and critical coupling (minimum transmission) was achieved at a 100 nm gap.*

To find the optimal coupling point we used Lumerical to simulate the transmission of light through a waveguide as it passes near a microdisk, varying the separating distance from 0  $\mu\text{m}$  to 1.4  $\mu\text{m}$ . We found that for a 500  $\mu\text{m}$  radius microdisk light begins to couple into the microdisk with a 500 nm coupling gap and the minimum transmission is reached with a 100 nm coupling gap. Taking the slope between 20% and 80% transmission we found that transmission changes by 0.340% for each nanometre change in coupling gap.

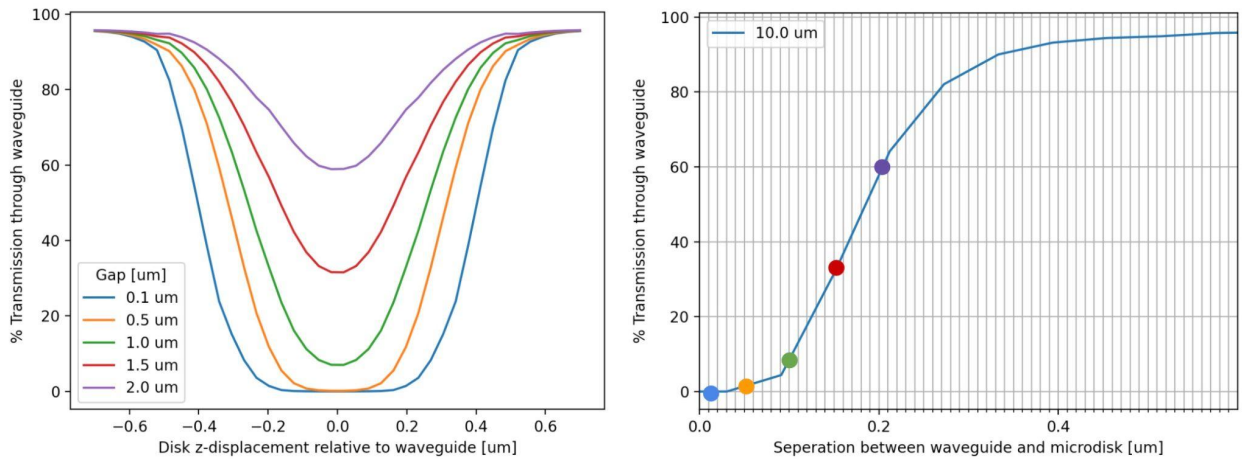


*Figure 14: Plot of the transmission of light through the waveguide as a function of vertical displacement between the waveguide and a 10  $\mu\text{m}$  microdisk for several fixed coupling gaps (left). The specific gaps are indicated on the 10  $\mu\text{m}$  coupling gap plot (right). Smaller coupling gaps have steeper transmission curves but a large region of zero change in transmission.*

Next, we looked at how the transmission changed when we varied the vertical distance between the waveguide and the microdisk. The results demonstrate that as the coupling gap increases, the change in transmission gets smaller for the same vertical displacement and the minimum transmission increases. Another key finding is that near zero displacement, the slope of the transmission curve is zero. Because the waveguide and disk are the same thickness, there needs to be a large offset to be able to measure a change in transmission. This is problematic since currently the displacements of the microdisks are only several picometers large. We can work around this issue by fabricating the microdisk at a vertical offset to the waveguide so that any oscillations will immediately yield changes in transmission.

## Chip Design

The chip design is motivated mainly by our sponsor's requirement for having a high-throughput system while also being useful for testing the new microdisk geometries and the evanescent coupling system. Therefore the 15mm x 15mm chip hosts an array of as many microdisks that can fit on the chip while the design still meets the design requirements that are outlined in this section. On the chip each microdisk is paired with an evanescent coupling subsystem that consists of a waveguide and two grating couplers (see Figure 15) to create what we call a cell. The grating couplers are devices fabricated onto the disk that allow light to pass through them in one direction without letting any light go in the opposite direction, similar to how a diode functions. One grating coupler couples light into the waveguide, while the other couples light out of the waveguide and off the disk into a photodetector.

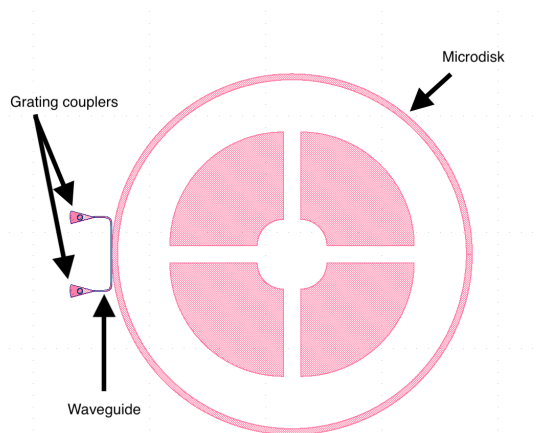


*Figure 15: Microdisk cell for repeating across the chip.*

The design constraints for the chip come from the chip dimensions, fabrication and testing requirements, and optical laws. The pattern is restricted to a 12mm x 12mm footprint centred on the chip rather than going right to the edges so that there is space to grip the chip during fabrication and while moving it around for testing. This helps prevent the devices that are fabricated onto the disk from getting damaged when the chip is being handled. The grating couplers must all be oriented the same way and be spaced 127  $\mu\text{m}$  apart from each other.

Orienting the grating couplers the same way enables the person performing tests to easily move from disk to disk without having to reorient the chip each time a measurement is performed. The spacing between the grating couplers matches the spacing between the probes that are used at the testing station the chip is designed for. The probes connect to the chip to input light and receive the ringdown signal from the tests. The waveguides have a pre-existing requirement of having a bend radius of at least 15 nm so that light can reflect effectively through their turns. In terms of microdisk oscillations, the spacing between the disks was not a concern since the oscillations of one microdisk would not be able to influence the oscillations of the others due to the substrate being absorbent enough to dissipate any energy lost into it before reaching the neighbouring disks outside the radius of the disk itself. When considering microdisk spacing with regard to evanescent coupling, the disks had to be more than 500 nm apart to ensure no coupling would occur between them, based on the results from the waveguide-microdisk coupling gap simulations. Using these restrictions, the cells were designed and repeated in an array over the footprint.

Initially there were 4 quadrants of disks (see Figure 16 below) on the chip so that each quadrant could be fabricated individually at different times so that if there was a mistake made while fabricating one of the quadrants it would not impact the others. The new design omits this because the fabricators have improved their fabrication techniques and are confident they can fabricate a continuous array of cells without mistakes, and therefore each chip will have more disks to perform more tests than the original design did.

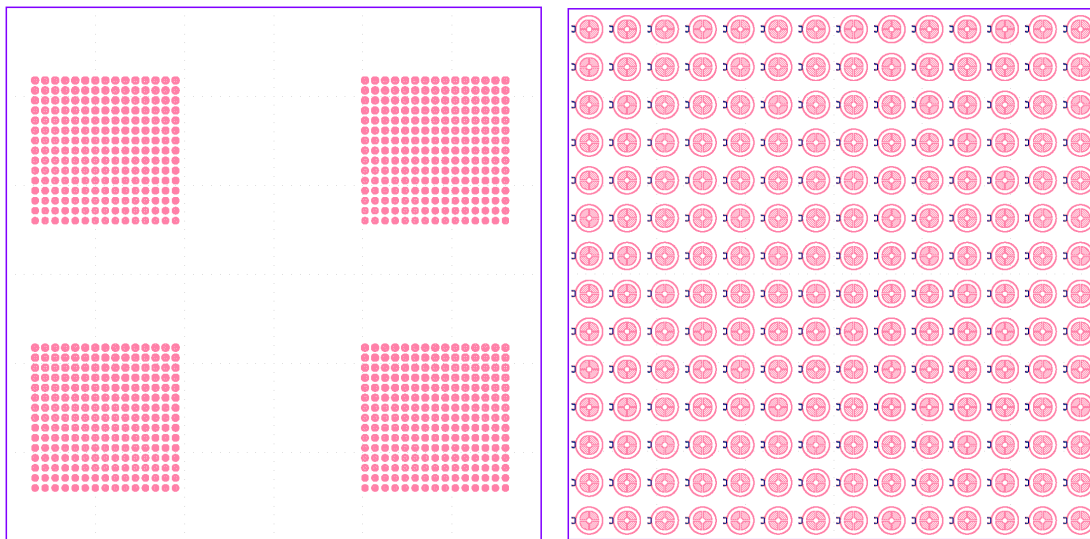


*Figure 16: Left: The original quadrant chip design. Right: The new, continuous chip design.*

Developing the chip design was done using python scripting in a program called [K-Layout](#) with the [SiEPIC-Tools extension](#). K-Layout allows the design to be exported and used directly for the fabrication method done by our sponsors. The script was developed by combining and modifying code for the original quadrant chip design with a modified sample code from the SiEPIC-Tools library. For this project two chip designs were developed: one to test the coupling gap, and one for testing coatings once the optimal coupling gap has been determined. The

coupling gap chip takes input for a high and low bound on the coupling gaps to test, and varies between those across the chip, as well as taking a disk radius argument. The coating test chip takes coupling gap and disk radius arguments and produces a chip with those parameters consistent across it to be able to test different coatings on consistent cells. Both scripts can be easily modified to produce chips with different microdisk designs by replacing the method that gets called to draw each disk with one for another design.

## Signal Processing

To prepare for making physical measurements on microresonators, we assembled an experimental setup that would produce modulated optical signals with a wavelength of 1550 nm. An overview of the setup and components is shown in Figure 17.

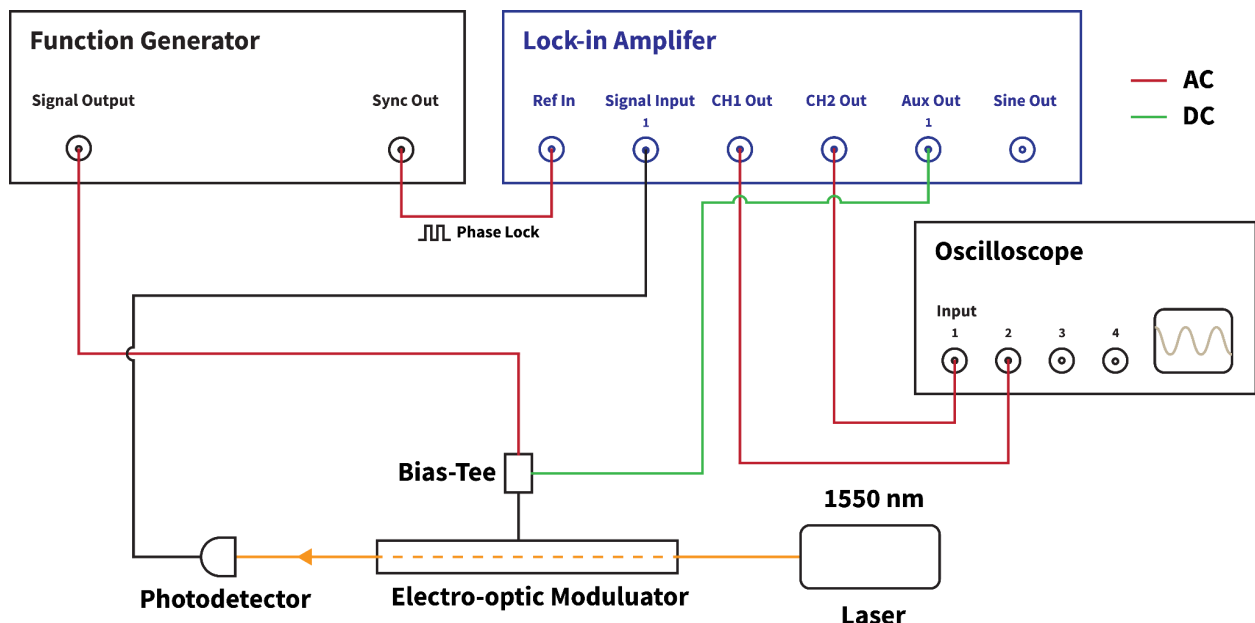


*Figure 17: The signal processing system overview. The HP81689A tunable laser acted as a 1550 nm wavelength light source. The laser light passes through an optical fiber and gets coupled into the Lucent X-2623Y electro-optic modulator. The modulator is driven by an internally modulated AC signal from the HP 3325B function generator, and a DC signal from an auxiliary output channel of the SR850 Lock-in amplifier. Modulated light exits the electro-optic modulator, and enters a Thorlabs DET01CFC photodetector. The output voltage of the photodetector is AC coupled into the signal input of the lock-in amplifier, which demodulates this into an in-phase and out-of-phase component. The in phase and out of phase components (at CH1 and CH2 output of the lock-in) are then read by a Keysight Infinivision 2024A DSO.*

Before testing, we determined appropriate operating ranges for the laser, intensity modulator, and the photodetector to prevent damage. These specifications are tabulated in Appendix J.

Our motivations behind assembling the setup were:

1. To allow for testing data acquisition scripts to be used in actual measurement.

2. To estimate the signal-to-noise ratio of the actual measurement setting as a function of the laser power, amplitude/frequency of the modulation signal, and amplitude/frequency of the carrier signal.
3. To experiment with methods of envelope extraction.

We will discuss our approach to accomplishing each of these goals, the instruments used, and the results.

#### Data acquisition

Our goal for data acquisition was to be able to make measurements of a voltage signal from a photodetector over time. Recall that as the microresonators ringdown, the transmission through the waveguide also oscillates in time. Since the voltage measured is proportional to the intensity of light, which is proportional to the amount of light transmitted, the voltage reading from the photodetector is a direct quantification of the level of transmission.

To do this, we decided to use the Keysight Infinivision 2024A oscilloscope over a traditional ADC such as the NI-DAQ, for the ability to visualise at most four inputs/outputs of the system in real-time. We chose python for facilitating the data acquisition because of our familiarity with the language, and also the many existing open-source packages for data acquisition and analysis, allowing the acquisition and analysis to be performed in a single environment.

Our software implementation extended upon the functionalities of the keyosc acquire package (*Keyoscacquire Documentation*, 2022) to be able to control the time/voltage per divisions and to control and acquire segmented waveforms. We expect our code can be easily integrated into a structured data acquisition framework such as QCoDeS (QCoDeS/Qcodes: *Modular Data Acquisition Framework*) in the future.

#### Signal-to-noise ratio measurement

To simulate a modulated optical signal, we used an HP laser module to provide a light source, with optical power as low as 100 uW.

To modulate the laser light, we used an intensity modulator. The electro-optical intensity modulator works by splitting the input beam into two paths (in a Mach-Zehnder configuration (*Mach-Zehnder Interferometer*)). Along one of the two paths, the beam passes through a lithium niobate crystal, whose refractive index changes with the strength of an applied electric field (*Electro-Optic Modulator*), causing a phase shift in the beam as the electric field varies. The two beams interfere with each other when they are recombined at the output.

The modulator was driven using an AC signal with a DC offset. The AC signal determines the waveform of the modulated light, and the DC signal sets the operating point of the modulator (determines what is the background refractive index in the crystal when there is no AC voltage applied).

To determine an operating point for the modulator at a specific drive frequency, we monitored the output of the photodetector by directly connecting the photodetector output to a channel of the oscilloscope (DC coupled). During testing, we found that for a fixed DC voltage, the shape of the modulated waveform changed with the AC drive frequency. Every time we wished to experiment with a different frequency, we tuned the DC voltage such that the waveform showed the least distortion and highest signal amplitude.

Using the setup proposed in Figure 17, we found during testing that no tuning of the AC/DC drive amplitudes or frequency could increase the photodetector voltage modulation beyond the order of tens of mV, in a DC background  $\sim 10$  V. We found that by removing the bias tee from the setup , and directly providing the AC/DC drive signal from the function generator alone increased the voltage modulation to several volts.

We can think about the amplitude ringdown of a resonator (illustrated in Figure 18 a)) as an amplitude modulated signal at the eigenfrequency of the resonator (or double the eigenfrequency in Figure 18 a), modulated by an exponentially decaying envelope. To simulate this behaviour, we drove the modulator using an amplitude-modulated AC signal produced by the HP 3325B function generator. Limited by the capabilities of the function generator, we could not directly synthesise a sinusoid with a decaying exponential envelope.

To determine the noise floor, we estimated the power spectral density (PSD) of the signal and found the region where the spectrum settles down to a particular frequency. To find the signal to-noise ratio, we compared the spectral peaks at the signal frequency versus the value of the PSD at the noise floor. This process is illustrated in Figure 18. For a derivation of how the power spectral density is an estimate of system noise, please refer to Appendix K.

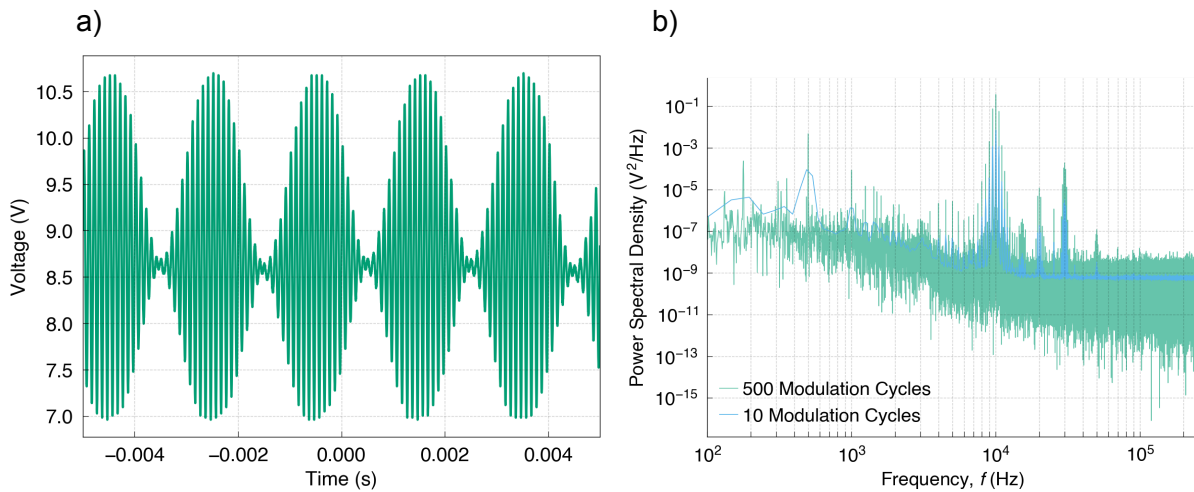


*Figure 18: (a): voltage signal from the photodetector seen on the oscilloscope. We configured the laser to output 100  $\mu$ W of power. The modulator was driven using a 0.17 V DC voltage. The AC signal used to drive the modulator was a 10 kHz signal, 2 Vpp, modulated by a 500 Hz signal from the internal modulation source of the function generator. The 500 Hz signal was configured to have a 12 Vpp amplitude for maximum modulation depth. (b): estimated power*

*spectral density. The green trace is estimated using the 500 modulation cycles, using a Hann window. The blue trace is estimated by truncating the data into 10 modulation cycles and averaging over separated PSD computed over each segment. The signal-to-noise ratio at 10 kHz is  $10^{-1}/10^{-9} \sim 10^8$ .*

#### Envelope extraction by lock-in demodulation

Measuring the ringdown time of an oscillator comes down to being able to extract the exponentially decaying amplitude envelope. One method we considered was to phase lock a lock-in amplifier to the carrier frequency of the function generator. To understand how a lock-in amplifier works in detail, we refer the reader to the references (Stanford Research Systems, 2020) and (Zurich Instruments, 2016). Details on tuning the lock-in parameters can be found in references (Stanford Research Systems, 2020) and (Zurich Instruments, 2019).

This method is particularly advantageous since the envelope of the voltage signal from the photodetector can be extracted in real time. For high Quality Factor resonators, high-frequency resonators, for which the ringdown envelope can extend  $> 10$  seconds, attempts to acquire the full waveform with a sufficiently large sampling frequency can become challenging. Real-time demodulation overcomes the need to sample data at a high frequency for a long period of time to get enough data for offline envelope extraction. The lock-in also provides built-in signal amplification, allowing us to measure signals before the mV range, and frequencies up to 100 kHz. But this comes with the cost of added system complexity and possibly lower throughput. For example, the lock-in parameters such as the time constant and phase must be tuned every time we switch between resonators that have different eigenfrequencies.

We demonstrate demodulating a sinusoidal envelope using the lock-in amplifier and how we tuned the lock-in parameters in Appendix L.

#### Envelope extraction by analytic signal

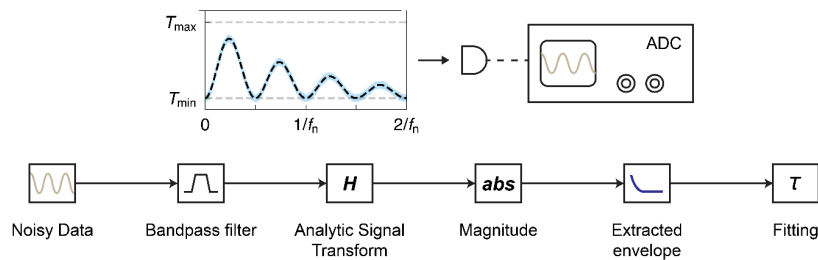


*Figure 19: Ringdown time extraction via analytic signal. The noisy experimental data acquired from an ADC is saved onto a computer. The data is band-pass filtered at the signal frequency. The filtered data is used to compute the analytic signal, which can be found by taking the Fourier Transform of the signal, removing all negative frequency components, followed by the Inverse Fourier Transform. Taking the magnitude of the analytic signal returns the signal envelope. We fit the extracted envelope to an exponential using the method of least squares to determine the ringdown time.*

Alternative to extracting the exponential decay envelope in real-time, one method of offline extraction we considered was to first filter the noise time series data at the signal by computing the “analytic signal” of the time series. The process is illustrated in Figure 19. Our implementation of this process can be found in the group GitHub repository: [https://GitHub.com/ligo-2205/ligo\\_measure/](https://GitHub.com/ligo-2205/ligo_measure/).

In simple terms, the analytic signal extends a real-valued signal into the complex plane. In this way, each point of the time series data can now be represented as a vector in the complex plane. To get the envelope, or the time-varying amplitude of the signal, we simply have to take the magnitude of the analytic signal. Using this method, we can also estimate the instantaneous phase and frequency of the signal. This processing is shown in the GitHub repository. The precise mathematical formulation of the idea can be found in the reference (*Analytic Signal*).

We tested this envelope extraction method using computer-generated data, where we have full control over the shape and noise level of the waveform, according to the following equation:

$$y(t) = Ae^{-t/\tau} \sin^2(2\pi ft) + B + N(0, \sigma^2)$$

where  $A$  represents the amplitude of the sinusoid (also called initial excitation in Figure 20),  $B$  is the DC component of the voltage signal, representing the minimum signal transmission,  $f$  is the frequency of the sinusoid,  $t$  is time,  $\tau$  is the ringdown time, and  $N(0, \sigma^2)$  is a zero-mean normal random variable with variance  $\sigma^2$ . We plot the distribution of the extracted ringdown time for various values of  $A$  and  $\sigma$  in Figure 20.

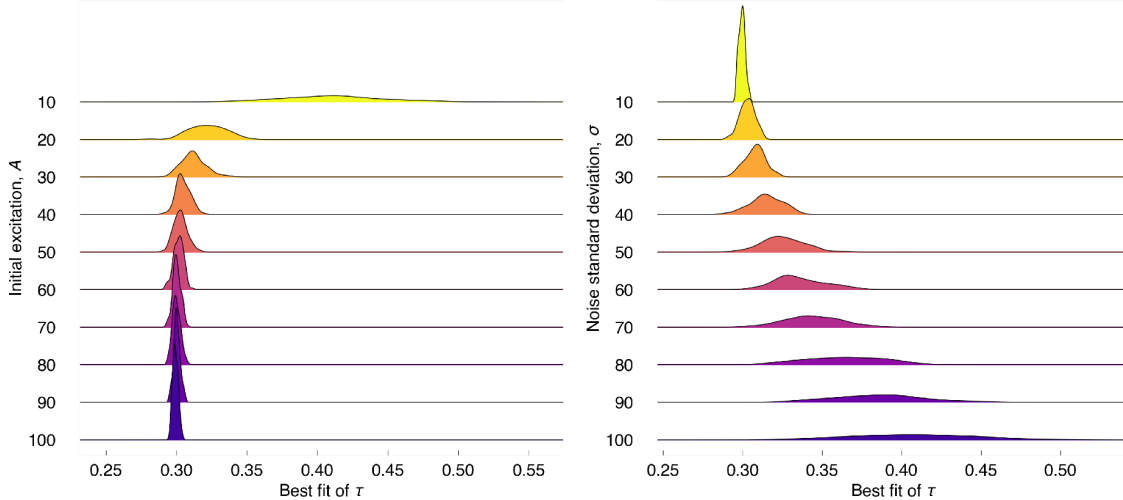


*Figure 20: For  $f = 10$  kHz,  $\tau = 0.3$ ,  $B = 200$ , the distributions of the best fit for  $\tau$  as we vary  $A$  between 10 and 100 for  $\sigma = 10$  (left), and as we vary  $\sigma$  between 10 and 100 for  $A = 100$  (right).*

We first applied a 6th order bandpass filter with a bandwidth of 50 Hz to the raw generated signal before performing the envelope extraction. We see that excess noise can cause the mean of the distribution for the ringdown time to disperse and shift to the right even when  $\sigma$  is only three-tenths of  $A$ . In the plot on the right, as  $A$  becomes comparable to  $\sigma$ , the distribution in the ringdown time also begins to disperse. This highlights the need to maximise the signal-to-noise ratio of the measurement setup .

## Conclusion

In this report, we demonstrated the first steps to realising a new thin-film coating measurement system that uses evanescent coupling to measure coating mechanical loss of thin films on microdisks. We created two microdisk designs stemming from the original design with physical theory and COMSOL simulations to lower their eigenfrequencies. The evanescent coupling system was incorporated with the microdisk measurement system, and fine-tuned using both COMSOL and Lumerical simulations to ensure the waveguides did not share eigenfrequencies with the microdisks, and to find the optimal evanescent coupling gap between the waveguides and microdisks. The results from these simulations were combined to produce two chip designs: one to test the coupling gap, and one that will be usable for testing thin-film coatings once the optimal real-world coupling gap has been determined. Finally, we assembled a physical prototype to simulate modulation of optical signals, and software to perform noise characterization, filtering, fitting, and data acquisition. We list recommendations and next steps in the section below.

## Recommendations

### Microdisks:

For the current design the sponsors use, we recommend adjusting the parameters as follows.

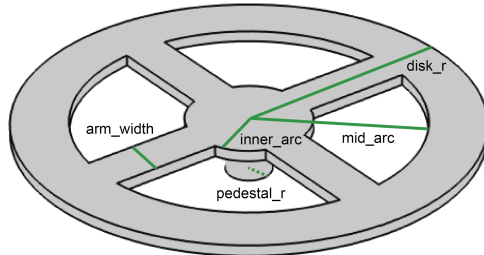


Figure 21: Original microdisk design with parameters labelled.

Table 2: Original microdisk design current parameter values versus recommended values.

Parameter	Current Value	Recommendation
disk_r:	80 $\mu\text{m}$	Maximise (500um?)
mid_arc_frac:	0.6	Tune to 0.7 - 0.8
inner_arc_frac:	0.25*disk_r	Minimise
pedestal_r:	0.25*disk_r	Minimise
arm_width:	0.05*disk_r	Minimise

For the hole design, we have decided on the below pattern as our recommendation, which has a simulated eigenfrequency of 3.11 kHz in vacuum. A full list of parameter values for this design can be found [here](#).

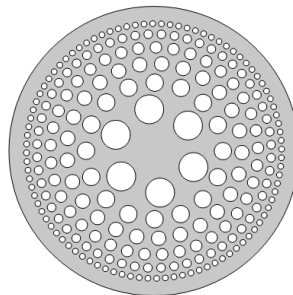


Figure 22: Final hole microdisk design

For the meander disk (Figure 7), more simulations using the code provided at [https://GitHub.com/ligo-2205/py\\_eigensim](https://GitHub.com/ligo-2205/py_eigensim) is required.

## Next steps:

For all three of the recommended microdisk designs, it is important to simulate the Q-factor of each to ensure we are still seeing high enough values. This would entail finishing creating the Q-factor simulation files and running them on the new designs (and original optimised design). For the Q-factor simulation files, an appropriately sized PML, substrate and meshing need to be determined.

After Q-factor simulations, for the original optimised design, the next steps would be to fabricate these disks in-lab, and do parameter sweeps varying one parameter at a time to determine realistic maximums and minimums for the values shown in the table above. These will be determined by analysing their mechanical limits (when they start to break in fabrication or when in oscillation). Once these values are determined, simulations should be performed in COMSOL to obtain expected eigenfrequencies with these updated parameters.

After Q-factor simulations, for the hole microdisk design, the next step would be to fabricate these disks in-lab. It would be beneficial to test a range of hole sizes in the radial direction and vary the number of holes in the angular direction all on one chip. Looking at if they break in fabrication or when vibrating we can test which structures are mechanically stable and adjust the designs as needed. Iteration will likely be necessary between fabricating sweeps of designs, and re-simulating to account for breakage/failure. After a design has been found to survive fabrication, it should be re-simulated in COMSOL to determine its expected eigenfrequency in vacuum.

## Waveguide

*Table 3: Waveguide recommendations*

Height [um]	500 nm
Width [um]	140 nm - 160 nm
Length [um]	200 $\mu$ m

## Next steps

In order to validate the results of the simulation we recommend that the sponsors fabricate a chip with a sweep of different exposed waveguide lengths (100  $\mu$ m - 200  $\mu$ m) to confirm if they are mechanically stable. They can also use the LDV system to measure if there are any vibrations of the waveguides when the chips are oscillating at the eigenfrequencies of the microdisks.

## Evanescnt coupling

*Table 4: Evanescnt coupling recommendations for a 500  $\mu\text{m}$  disk*

Mode	Transverse magnetic
Coupling gap	< 100 nm
Vertical displacement	Centred so that at equilibrium there is 50% transmission

### Next steps

Running the 3D simulations for 500  $\mu\text{m}$  disks takes longer than 12 hours for 500  $\mu\text{m}$  disks. We recommend repeating the height sweeps for larger disks (50  $\mu\text{m}$  and 100  $\mu\text{m}$  to start) to see if the changes in transmission occur at the same heights.

Next, to validate the results of the simulations we recommend fabricating a chip where the gap between the microdisk and the waveguide is varied from 50 nm to 300 nm and measuring the transmission for each gap. Once the gap that minimises transmission is identified, we recommend fabricating a chip with that horizontal gap and with a vertical offset between the waveguide and the microdisk. The waveguide should be between 200 nm and 500 nm below the microdisk.

## Chip Design

Considering the values we found during our coupling gap simulations, we recommend first using the coupling gap chip with a lower bound of 100 nm, and a higher bound of 300 nm to find the optimal real-world coupling gap. Additionally, we recommend testing the coupling gaps with different radii to see whether the disk size impacts the evanescent coupling. Once the coupling gap has been finalised, we recommend using the coating tester chip design to further test variations of our new microdisk geometries before using it for coating testing.

### Next steps

Once it is determined which microdisk designs can withstand fabrication, the next steps for the chip design would be to develop scripts to generate the resilient disk designs and replace the function that calls the spoked disk design with the new scripts to facilitate testing with them.

## Signal Processing

For future work, students should continue to explore both the real-time and offline envelope extraction methods, all while maximising the signal-to-noise ratio of the measurement setup.

From Q-factor simulations/measurements of fabricated resonators in vacuum, future work may require continuously acquiring data at a modest sampling frequency (1 kHz to 10 kHz) for an extended period of time (> 10 seconds) to record the entire ringdown signal.

## Deliverables

1. Microdisk designs
  - a. Python script to automate running simple eigenfrequency simulation over simple GDS files ([https://GitHub.com/ligo-2205/py\\_eigensim](https://GitHub.com/ligo-2205/py_eigensim))
  - b. Optimised original design recommendations (Table 2)
  - c. Final hole design recommendation
    - i. List of parameters, eigenfrequencies and an image (found in [here](#), labelled Hole Design Parameters, Hole Design Eigenfrequencies, and Hole Design Image)
    - ii. COMSOL file containing this design (microdisks\_geometry\_hole\_design.mph)
  - d. Hole design and optimised original design integrated into Q-factor simulation file
    - i. Hole design COMSOL file (Q\_Factor\_Hole\_Design.mph)
    - ii. Optimised original design COMSOL file (Q\_Factor\_Original\_Optimized\_Design.mph)
  - e. Instruction doc outlining key components of the hand-off files ([COMSOL Files Instructions](#))
2. Waveguide
  - a. Waveguide design recommendations (Table 3)
  - b. COMSOL file used for waveguide simulations ([Waveguide.mph](#))
3. Coupling gap simulations
  - a. Coupling gap design recommendations (Table 4)
  - b. Lumerical file, setup to run gap and height sweeps for 500 µm microdisks ([500um\\_disk\\_coupling.fsp](#))
4. Chip design
  - a. Python script to generate chip to test the coupling gap, takes disk radius and a top and bottom limit for the coupling gaps to test (LIGO\_chip\_coupling\_gap\_test\_FINAL.py)
  - b. Python script to generate chip designs with the spoked disk design, takes radius and coupling gap as arguments (LIGO\_chip\_design\_FINAL.py)
  - c. Instructions for how to modify scripts to change cell spacing and the microdisk design in the code ( [Chip design script instructions](#) )
5. Signal processing ([https://GitHub.com/ligo-2205/ligo\\_measure](https://GitHub.com/ligo-2205/ligo_measure))
  - a. Python script for
    - i. Data acquisition using Keysight 2024A DSO
    - ii. Frequency domain analysis of signals, such as filtering, power spectral density, and signal-to-noise ratio computation

## Works Cited

- Alem, M. (2017, March 29). *Noise Analysis of Signal Components*. Zurich Instruments.  
<https://www.zhinst.com/americas/en/mehdia/2017/03/29/noise-analysis-of-signal-components>
- Analytic Signal. (n.d.). Wikipedia. [https://en.wikipedia.org/wiki/Analytic\\_signal](https://en.wikipedia.org/wiki/Analytic_signal)
- COMSOL. (2018, April 19). *Eigenfrequency Analysis*. Multiphysics Cyclopedia. Retrieved April 1, 2022, from <https://www.comsol.com/multiphysics/eigenfrequency-analysis>
- Daendliker, R. (2000, June 16). *Concept of modes in optics and photonics*. Sixth International Conference on Education and Training in Optics and Photonics, 6.
- Electro-optic modulator. (n.d.). Wikipedia. Retrieved April 9, 2022, from  
[https://en.wikipedia.org/wiki/Electro-optic\\_modulator](https://en.wikipedia.org/wiki/Electro-optic_modulator)
- Falco Systems. (2018, April). *Quick and dirty MEMS design*. Falco Systems. Retrieved April 9, 2022, from [http://www.falco-systems.com/quick\\_MEMS.pdf](http://www.falco-systems.com/quick_MEMS.pdf)
- Granata, M., Amato, A., Cagnoli, G., Coulon, M., Degallaix, J., Forest, D., Mereni, L., Michel, C., Pinard, L., Sassolas, B., & Teillon, J. (2020). Progress in the measurement and reduction of thermal noise in optical coatings for gravitational-wave detectors. *Applied Optics*, 59(5), A229.  
<https://doi.org/10.1364/AO.377293>
- Gumelar, M. R., & Purnamaningsih, R. W. (2019). The Effects of Ring Radius and Coupling Gap on the Transmission Spectrum of GaN-Based Ring Resonator. *16th International Conference on Quality in Research (QIR): International Symposium on Electrical and Computer Engineering*, 1-4.
- keyoscacquire Documentation. (2022). keyoscacquire.  
<https://keyoscacquire.readthedocs.io/en/stable/>
- Li, T., Sandoval, F. A. A., Geitner, M., Cagnoli, G., Dolique, V., Degallaix, J., Flaminio, R., Forest, D., Granata, M., Michel, C., Morgado, N., Pinard, L., & Bellon, L. (2014). Measurements of mechanical thermal noise and energy dissipation in optical dielectric coatings. *Physical Review D*, 89(9), 092004. <https://doi.org/10.1103/PhysRevD.89.092004>
- Mach-Zehnder interferometer. (n.d.). Wikipedia. Retrieved April 9, 2022, from  
[https://en.wikipedia.org/wiki/Mach%20Zehnder\\_interferometer](https://en.wikipedia.org/wiki/Mach%20Zehnder_interferometer)
- Musa, Sami & Borreman, Albert & Kok, Abigail & Diemeer, Mart & Driessen, Alfred. (2004). Experimental Study of Bent Multimode Optical Waveguides. *Applied optics*. 43. 5705-7.  
10.1364/AO.43.005705.
- Paschotta, R. (n.d.). Q factor. RP Photonics Encyclopedia. Retrieved April 1, 2022, from  
[https://www.rp-photonics.com/q\\_factor.html](https://www.rp-photonics.com/q_factor.html)
- QCoDeS/Qcodes: Modular data acquisition framework. (n.d.). GitHub. Retrieved April 9, 2022, from  
<https://GitHub.com/QCoDeS/Qcodes>
- Robertson, B. (2018, February 2018). *Optical Loss & Testing Overview*. Kingfisher International. Retrieved April 10, 2022, from  
<https://kingfisherfiber.com/application-notes/optical-loss-testing-overview/>

Stanford Research Systems. (2020, April 7). *Lock-in Basics*. thinkSRS.com. Retrieved April 9, 2022, from <https://www.thinksrs.com/downloads/pdfs/applicationnotes/Lock-In%20Basics.pdf>

Sun, X., Zhang, X., & Tang, H. X. (n.d.). *High-Q Silicon Optomechanical microdisk resonators at gigahertz frequencies*. Retrieved April 1, 2022, from <https://arxiv.org/pdf/1204.3605>

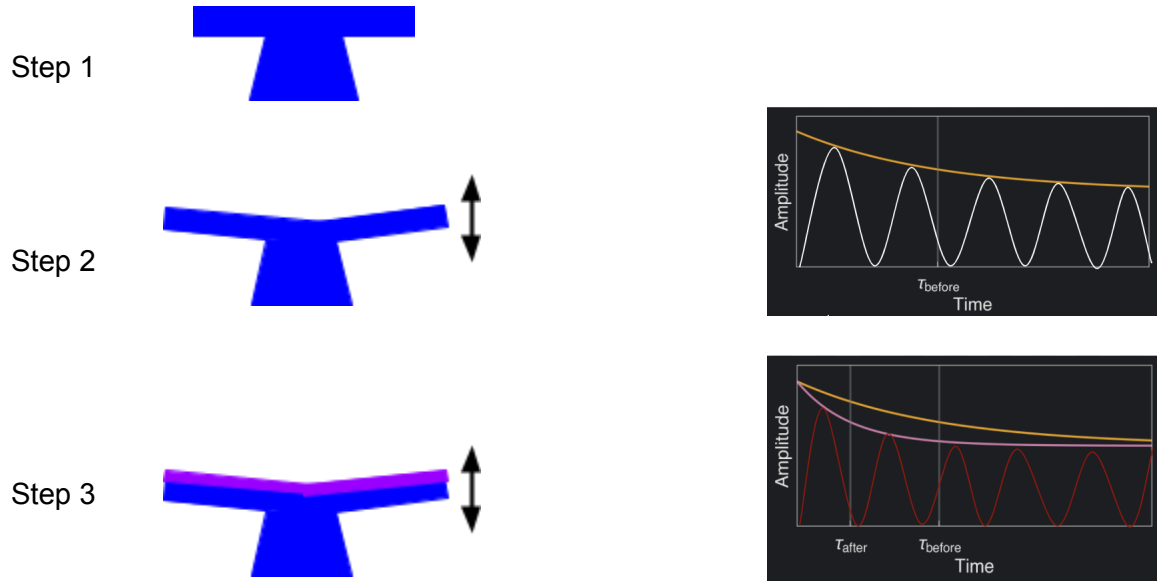
Zurich Instruments. (2016, November 21). *Principles of lock-in detection and the state of the art*. Zurich Instruments. Retrieved April 9, 2022, from [https://www.zhinst.com/sites/default/files/documents/2020-06/zi\\_whitepaper\\_principles\\_of\\_lock-in\\_detection.pdf](https://www.zhinst.com/sites/default/files/documents/2020-06/zi_whitepaper_principles_of_lock-in_detection.pdf)

Zurich Instruments. (2019, February 22). *6 Tips to Improve your Lock-in Amplifier Measurements*.

Youtube. <https://www.youtube.com/watch?v=vpulgJJDwP0&t=144s>

## Appendices

### Appendix A: Measuring mechanical loss using a resonator



Step 1 illustrates a stationary mechanical resonator structure. In Step 2, we use a driving force to create vibrations in the resonator at its natural frequency. We then turn off the driving force, allowing the oscillations to eventually fully dampen with time. This creates the decaying sinusoidal shown in the graph in line with step 2. We can then fit an envelope to that curve (shown in orange) and determine its ringdown ( $\tau_{before}$ ) which represents the time at which the amplitude is  $1/e$  times the original amplitude of the envelope. Next, we would follow the same process but this time the resonator would have a thin film applied on top of it (shown in purple in Step 3). We would be able to get a similar envelope for the thin film covered resonator (purple curve in the graph in line with Step 3), and similarly would obtain its ringdown ( $\tau_{after}$ ). The values  $\tau_{before}$  and  $\tau_{after}$  would then be used to calculate mechanical loss in the thin film.

## Appendix B: Original microdisk design optimization

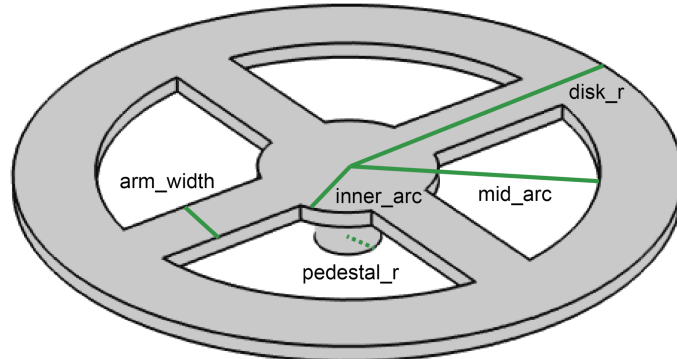


*Figure 23: Sponsor's current microdisk design labelled with parameters we varied in simulation.*

The parameters we tested and optimised for the original microdisk design used by our sponsors are depicted in the image above.

We started by varying the overall radius of the microdisk (`disk_r`) to study how eigenfrequency was impacted. Figure 24, below, illustrates the results of these tests. For this simulation specifically, we used values as follows:

- `arm_width = 0.05*disk_r`
- `pedestal_r = 0.1*disk_r`
- `inner_arc_frac = 0.25` (note `inner_arc = inner_arc_frac*disk_r`)
- `mid_arc_frac = 0.6` (note `mid_arc = mid_arc_frac*disk_r`)
- `disk_r` varying from 80  $\mu\text{m}$  to 1000  $\mu\text{m}$

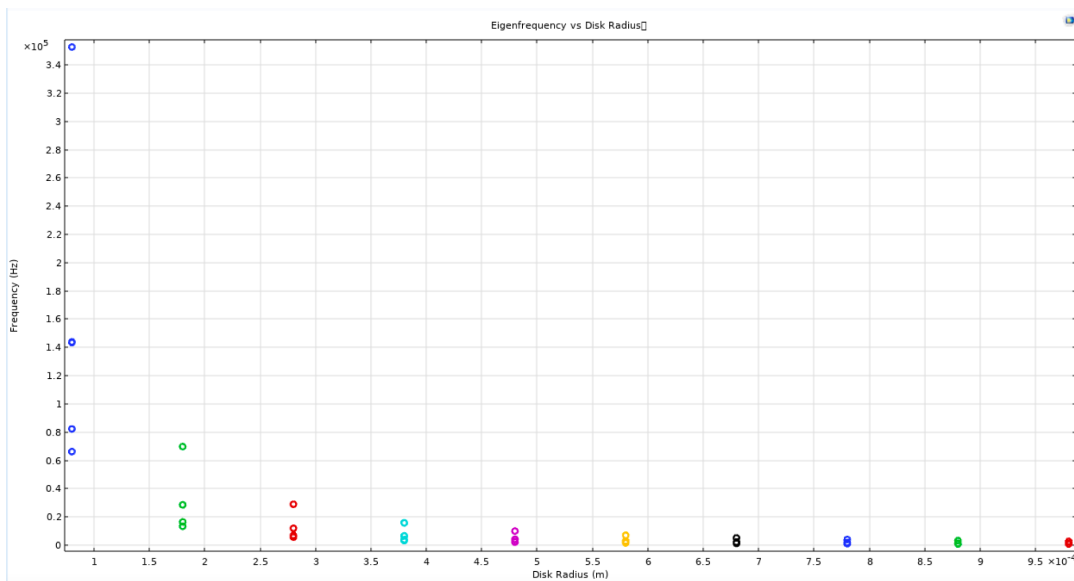


*Figure 24: Plot of eigenfrequency vs. disk radius for the sponsor's original microdisk design.*

*Eigenfrequency tends to decrease exponentially with increasing disk radius. Thus, our first method for greatly reducing the eigenfrequency of the microdisks was to design disks with as big a radius as possible. As previously mentioned, this number is 500  $\mu\text{m}$ .*

The next parameter we tested was mid\_arc\_frac, or in other words, the distance from the centre of the microdisk to the edge of the cutouts. This would determine the size of the cutouts. We found this value optimised between 0.7 and 0.8.

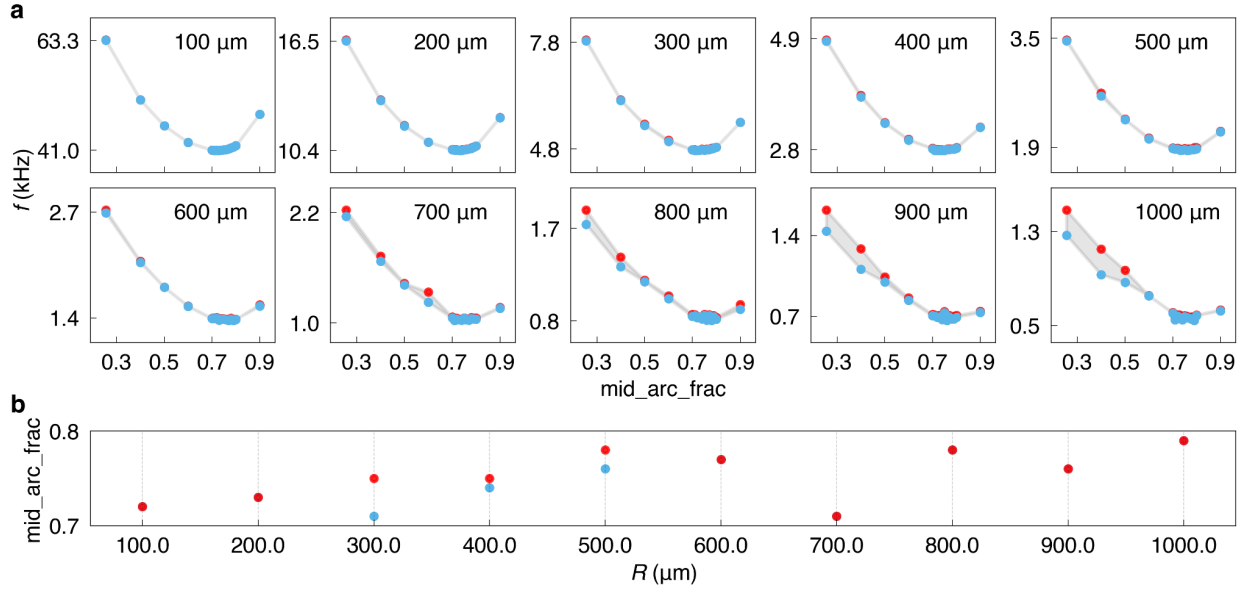
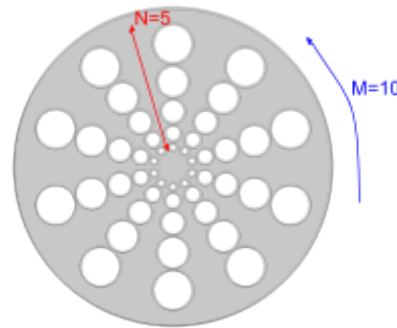


*Figure 25: (a): Eigenfrequencies of the first two eigenmodes as a function of mid\_arc\_frac, for disk radius between 100 to 1000  $\mu\text{m}$ . An eigenfrequency minimum was found between 0.7 to 0.8 in all cases, as highlighted in (b).*

The remaining adjustable parameters all provided similar results, being that minimising them would provide the lowest eigenfrequency.

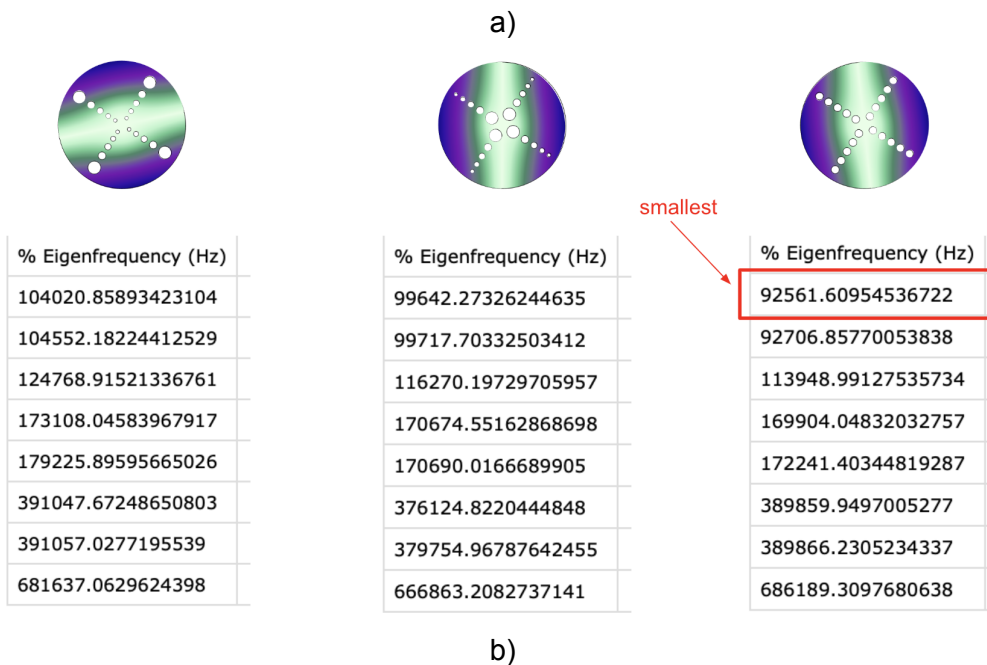
## Appendix C: Hole microdisk design

For this design, we varied the pattern, size, and number of hole cutouts in the microdisk. A general idea of what this design could look like is shown in Figure 26.



*Figure 26: Example of a possible hole cutout pattern for the new design.*

There are many parameters that can be varied with this design, including N (number of holes in the radial direction), M (number of holes in the angular direction, could be different for each hole going radially out), the size of each hole, and the spacing between holes (both radially and angularly). Rigorous testing was performed to determine which combinations provided the lowest eigenfrequencies. One of the more notable patterns discovered was that decreasing the hole radius going radially out (largest holes in the centre, getting smaller as you go out) provided a lower eigenfrequency than the reverse or having constant hole sizes, for which an analysis is shown below.



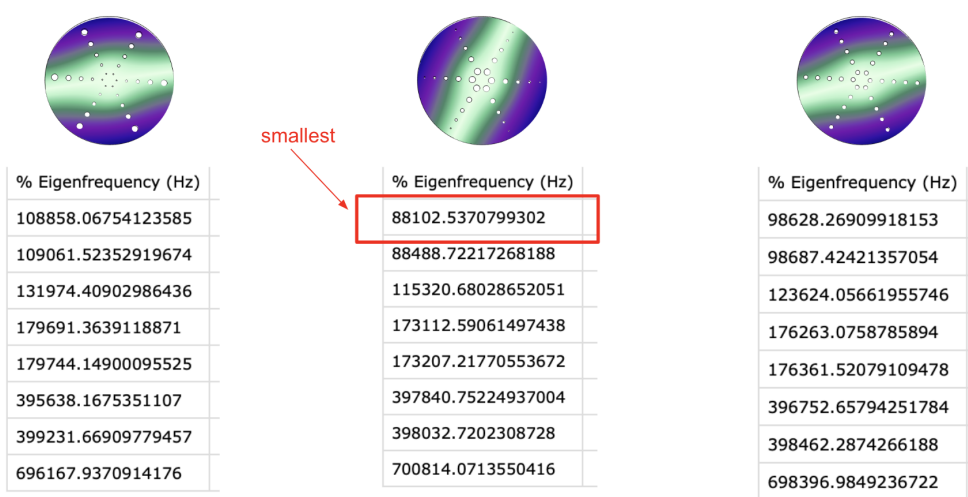
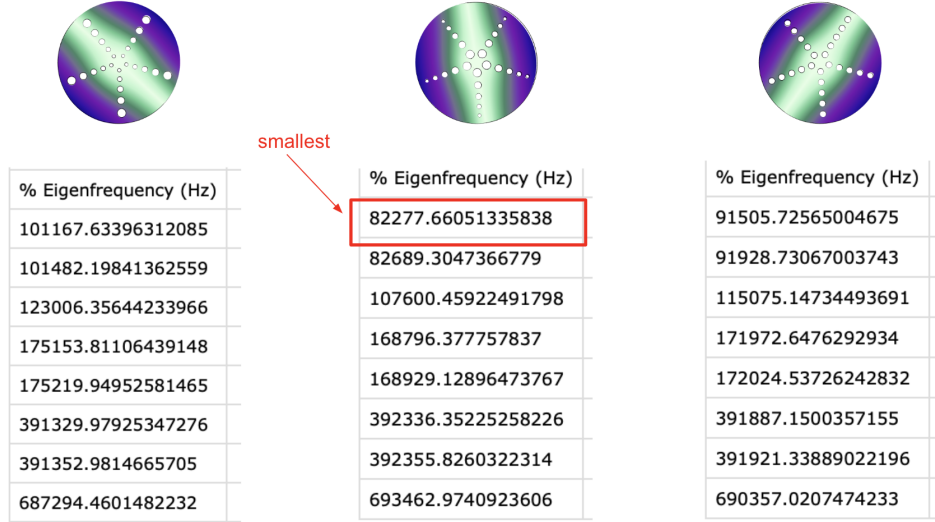


*Figure 27: Comparison between hole radii increasing vs. decreasing vs. remaining constant in the radial direction. We also varied the number of holes in angular direction across test sets, a) has 4, b) has 5, and c) has 6.*

Figure 27 demonstrates three separate simulations comparing the eigenfrequencies of the first eight modes for three distinct hole patterns: Increasing radii going radially out (left most), decreasing radii going radially out (centre), and radii remaining constant going radially out (right most). In a), there are four holes in the angular direction for each radial position, whereas in b) we increased that to five, and in c) we increased that to six. Within each of a), b), c), across the three patterns we kept the total amount of cut-out volume the same. You can see in a), having constant hole radii going radially outward produced the lowest eigenfrequency. However, when we increased the number of holes in the radial direction (as in b) and c)), we saw that having a pattern of decreasing hole radii in the radial direction produced the smallest eigenfrequency by a larger margin. Since our final design would have more angular holes than the designs shown above, we decided to move forward with the decreasing radii pattern going outwards in the

radial direction. These tests were done on an 80  $\mu\text{m}$  disk radius, and we are assuming results will hold for a 500  $\mu\text{m}$  disk radius (which will be used in our final design).

Next, the number of holes in the *angular* direction producing the lowest eigenfrequency varied based on how far out (radially) the hole was. For example, the innermost hole was optimal when there were four of them in the angular direction, whereas the outermost hole had a much higher number. There was not a direct correlation between increasing the amount of holes in the angular direction and having eigenfrequency decrease. In general, there was a specific number (between a maximum and minimum value) for each hole position that was optimal. However, by having too few holes in the angular direction, we ran into our aforementioned etching rate constraint. That is, if there were large parts of the disk without holes, we would run into the problem where our pedestal would be etched away by the HF before the disk was fully and properly undercut. Thus, even though having the maximum number of holes in the angular direction may have not provided the absolute lowest eigenfrequency, it was a necessary part of our design to meet that constraint. To further ensure that the pedestal supporting the disk is not compromised, in the final design the centre holes are moved a distance of 45  $\mu\text{m}$  out from the edge of the pedestal radius, which we calculated to be the appropriate distance to ensure at most 5  $\mu\text{m}$  of the pedestal radius gets etched away in fabrication. Our finalised first design is depicted below, for a list of parameter values see Appendix D. With this design, we were able to reduce the eigenfrequency to **3.11 kHz**.

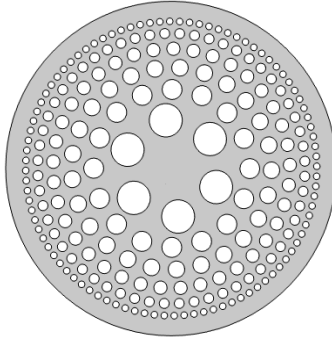


*Figure 28: Final recommended design for microdisk with many holes.*

## Appendix D: Finalised hole microdisk design parameters

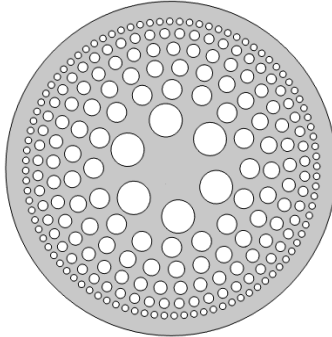


*Figure 29: Finalised hole design.*

The parameters below are some of the more significant parameters that describe the above design.

*Table 5: Hole design parameter recommendations*

Parameter	Value	Description
disk_r	500 [um]	Disk radius
pedestal_r	50 [um]	pedestal radius
N	6	# of holes in radial direction
etch_s	45 [um]	The amount of space to leave from the pedestal radius to the first hole so not all the pedestal gets etched away in fabrication
hole_r_1	50 [um]	Radius of innermost hole.
hole_r_2	30 [um]	Radius of hole 2.
hole_r_3	25 [um]	Radius of hole 3.
hole_r_4	20 [um]	Radius of hole 4.
hole_r_5	15 [um]	Radius of hole 5.
hole_r_6	10 [um]	Radius of outermost hole.
M_1	6	Number of holes in angular direction for innermost hole.
M_2	16	Number of holes in angular direction for hole 2

M_3	25	Number of holes in angular direction for hole 3
M_4	37	Number of holes in angular direction for hole 4
M_5	57	Number of holes in angular direction for hole 5
M_6	92	Number of holes in angular direction for outermost hole.
hole_s	11 [um]	Hole separation. Distance between each hole radially.

## Appendix E: Meander arms microdisk design

The second design we created looked to minimise the stiffness of the arms in the original design, thereby lowering the eigenfrequency of the resonator. Drawing inspiration from design of micro-springs in MEMS accelerometers, we proposed to replace the straight arms using a meander pattern. Two variations of the design are shown in Figure 30.

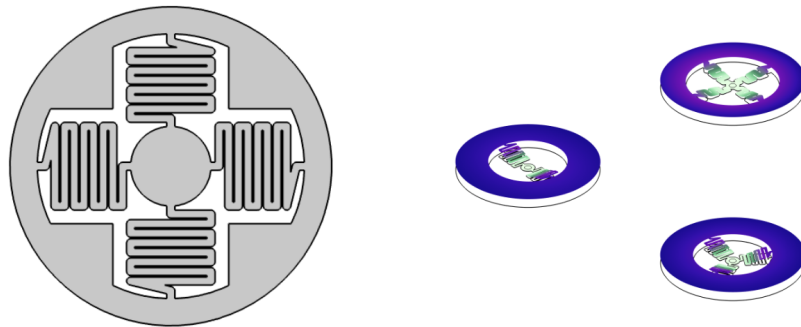


*Figure 30: Microdisk design with meandering arms expected to decrease the stiffness in each arm. Right: one variation of the meander design without the added mass along the outer ring, shown in their first eigenmode. Left: A second variation of the design.*

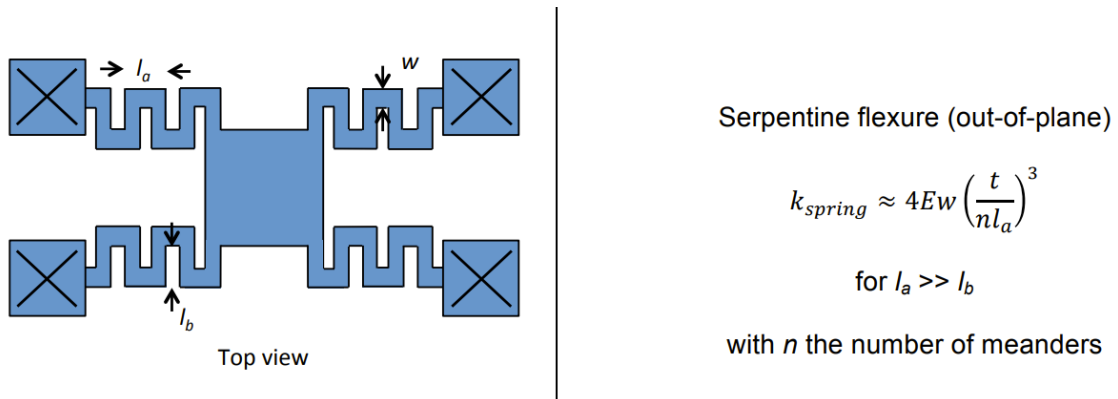


*Figure 31: Intuition behind the meander design. From the formula for the effective spring constant of the “serpentine flexure”, we see that it’s possible to greatly decrease the spring constant by increasing the number of turns in the meander. Adapted from (Falco Systems, 2018).*

## Appendix F: Calculating wavelength of an acoustic wave in silicon

To calculate the wavelength we know that  $\lambda = \frac{v}{f}$  where lambda is wavelength, v is the speed of sound in silicon, and f is the frequency of interest (in this case the lowest eigenfrequency of our microdisk). To get the speed of sound in silicon, we can perform  $v = \sqrt{\frac{\text{shear modulus}}{\text{density}}}$ , plugging in the corresponding values for silicon that COMSOL provides us with (or by looking them up). Speed of sound in silicon using this equation should come out to 5339.7 [m/s] using the following values:

- Young's modulus = 170GPa
- Poisson ratio = 0.28
- Density = 2329 kg/m<sup>2</sup>
- Shear modulus =  $\frac{\text{Young's modulus}}{2*(1+\text{poisson ratio})} = 66.4 \text{ GPa}$

## Appendix G: Optics and evanescent waves

The speed of light changes when it propagates in different media. This is why light refracts (bends) as it passes from one medium to another. The refractive index is a material property that is defined as the ratio of the speed of light in a vacuum to the speed of light in the material. Snell's law is the mathematical relationship that describes the bending of light as it is transmitted from one medium to another.

$$n_1 \sin(\theta_1) = n_2 \sin(\theta_2)$$

Where  $n_1$  and  $n_2$  are the indices of refraction of the first and second medium and  $\theta_1$  and  $\theta_2$  are the incident and refracted angle of the light with respect to the normal of the boundary between the 2 mediums.

$$\theta_2 = \arcsin \left[ \frac{n_1}{n_2} \sin(\theta_1) \right]$$

Rearranging equation x for the refracted angle  $\theta_2$ , we see that if  $n_1$  is greater than  $n_2$  and  $\theta_1$  is greater than some critical angle ( $\theta_c$ ) the argument of arcsin will be greater than 1 and there will be no real refracted angle. Under such conditions total internal reflection occurs, all of the light is reflected at the boundary and remains in the first medium. However, because light cannot be discontinuous at a boundary an evanescent wave will be generated on the far side of the medium boundary. It will not propagate and its strength will decay exponentially with distance from the boundary.

Consider three media with refractive indices such that  $n_1 < n_2$  and  $n_1 = n_3$ . If an incident beam of light in medium 1 hits the first boundary at an angle greater than the critical angle total internal reflection will occur and a decaying evanescent wave will be generated in the second medium. If the third medium is situated at a distance where the evanescent wave has not decayed some of the evanescent wave will penetrate into the third medium and light can begin to propagate through it.

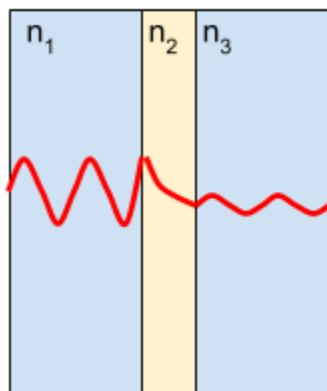


*Figure 32: Diagram depicting evanescent coupling. Light propagates in medium 1, when it arrives at the boundary with medium a decaying evanescent wave is generated. The evanescent wave arrives at medium 3 with lower total power and a propagating wave with less energy than the initial wave is generated.*

## Appendix H: Waveguide Design

We considered the 2 geometries pictured in Figure 33 to model the suspended waveguide. The first consists of the Si waveguide fixed to the top of two large  $\text{SiO}_2$  pillars. A fixed boundary condition was applied to the base face of both pillars. This was done to emulate the waveguides sitting on top of the  $\text{SiO}_2$  layer of the chip. The second model was simplified to a rectangular Si beam with the two end faces fixed.

Ultimately our simulations and analysis were done using the simplified model. Despite the simplification it is still an accurate model for the system because the size of the substrate and the length of the waveguides that extend over the  $\text{SiO}_2$  layer are very large relative to the length and size of the exposed waveguide we were interested in simulating. Furthermore, initial simulations were run with both models and the results were very similar so follow up analysis was done with the simplified model.

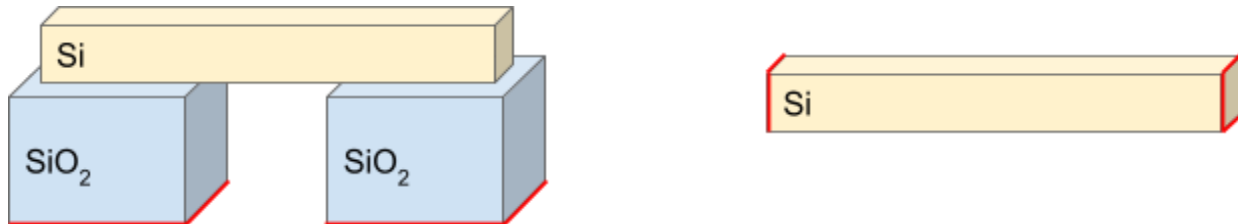


*Figure 33: Diagram of the two potential waveguide models. On the left, a rectangular beam silicon waveguide with two silicon dioxide pedestals. On the right, a rectangular beam silicon waveguide. The fixed boundary conditions of the model are indicated in red.*

To set up the model in COMSOL we created the waveguide structure using COMSOL's block tool. The waveguide block material is defined as Silicon from COMSOL's material library. It applies the key material properties of silicon to our simulation, its young's modulus being the most relevant to this simulation.

We set up 3 parameter sweeps using COMSOL's study tool. First, a mesh size sweep was implemented to verify the accuracy of the model. Then one sweep looked at the effect of changing the waveguide's length and the last sweep looked at the effect of changing the waveguide's width keeping all other parameters constant.

*Table 6: Parametric sweep parameters*

Parameter	Start	Step size	Stop
Number of mesh elements	10	5	60
Width	140 nm	6.67 nm	180 nm
Length	10 $\mu\text{m}$	5 $\mu\text{m}$	200 $\mu\text{m}$

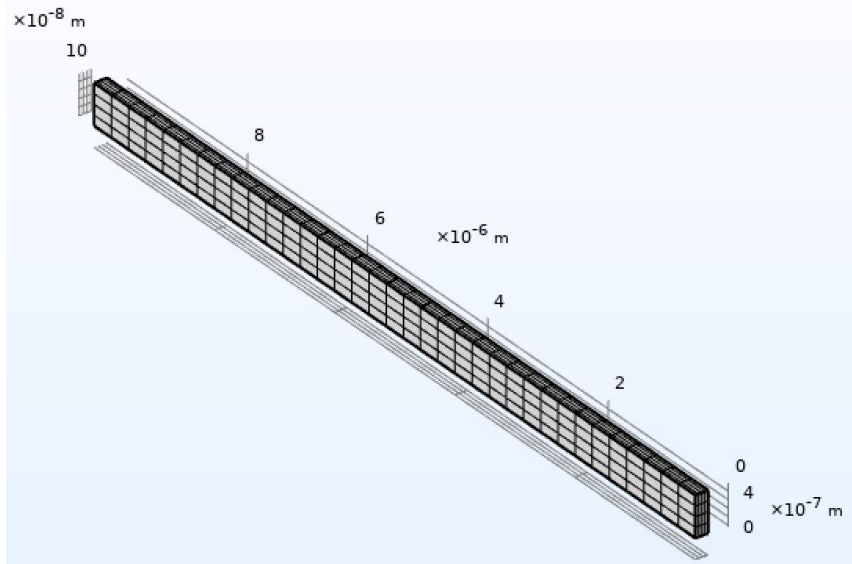


*Figure 34 : Image of the waveguide model from COMSOL with the swept mesh implemented.*

For this simulation we used a swept mesh instead of COMSOL's default tetrahedral mesh. With the tetrahedral mesh we ran into errors with the size of the mesh fitting the faces and thin edges of the waveguide. As a result we had to use really small element sizes which led to long simulations and we also found that this incorrect mesh resulted in imaginary eigenfrequencies when we ran the simulation. The swept mesh worked well with our geometry because we could explicitly define the size of each rectangular cell in a 2D plane and then extend it through to the rest of the beam.

To validate the accuracy of the model we ran a sweep of the number of mesh elements along the length of the beam. We found that, for all waveguide lengths, the eigenfrequencies computed by the simulation converge for greater than 30 elements.

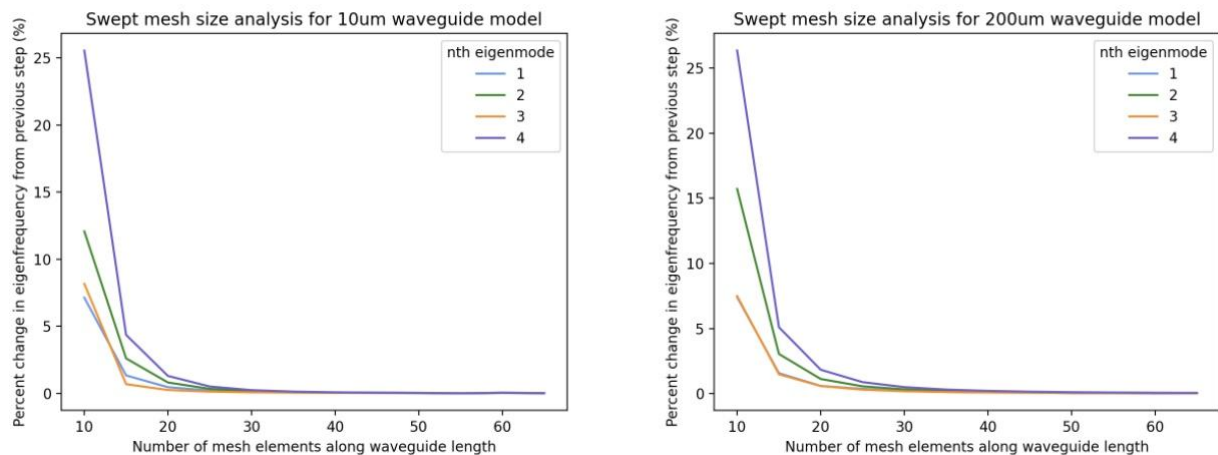


*Figure 35: Plots showing the change in eigenfrequency computed as a function of mesh accuracy. For both 10  $\mu\text{m}$  (left) and 200  $\mu\text{m}$  (right) waveguides the eigenfrequencies computed by the simulation begin to converge at 30 elements.*

## Length results

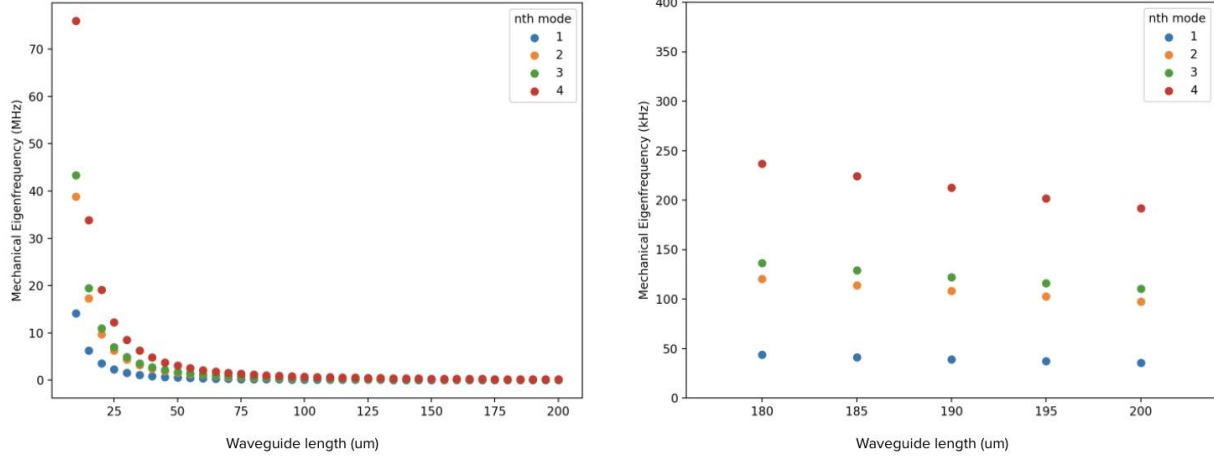


*Figure 36: On the left, eigenfrequency of first four eigenmodes of a fixed width (160 nm) waveguide as a function of length (10  $\mu\text{m}$  - 200  $\mu\text{m}$ ). On the right, eigenfrequencies at the upper length limit (180  $\mu\text{m}$  - 200  $\mu\text{m}$ ).*

The data in Figure 36 demonstrates that the eigenfrequency of the waveguide is inversely proportional to its length. In our design longer waveguides are ideal because that increases the length of the exposed evanescent waves that can couple into the microdisk. Looking at the upper range of lengths in the right plot of Figure 36 we see that the lowest eigenfrequencies measured are between 25 kHz - 50 kHz.

## Width data

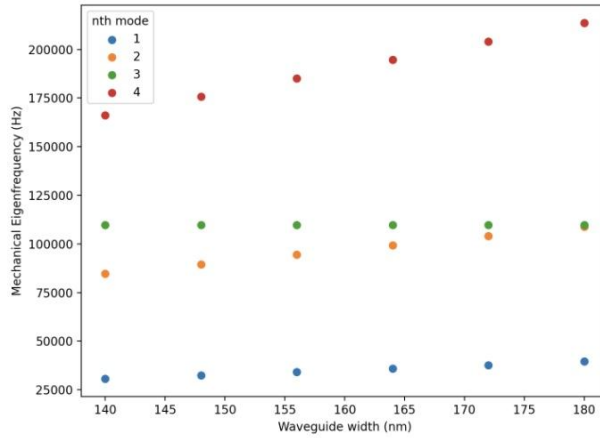


*Figure 37: Plot of waveguide eigenfrequency as a function of waveguide width for a 200  $\mu\text{m}$  long waveguide. The eigenfrequencies increase as the width of the waveguide increases.*

The eigenfrequency of the first four mechanical modes are plotted as a function of width. In Figure 37 we see a general trend that eigenfrequency increases linearly as width increases.

Increasing the width of the waveguide will increase both its mass and its stiffness. Since the waveguide is very thin the change in mass is less significant than the change in stiffness. The slope for each mode is different, likely a result of the different mode shapes that satisfy the model's boundary conditions.

### Other comments

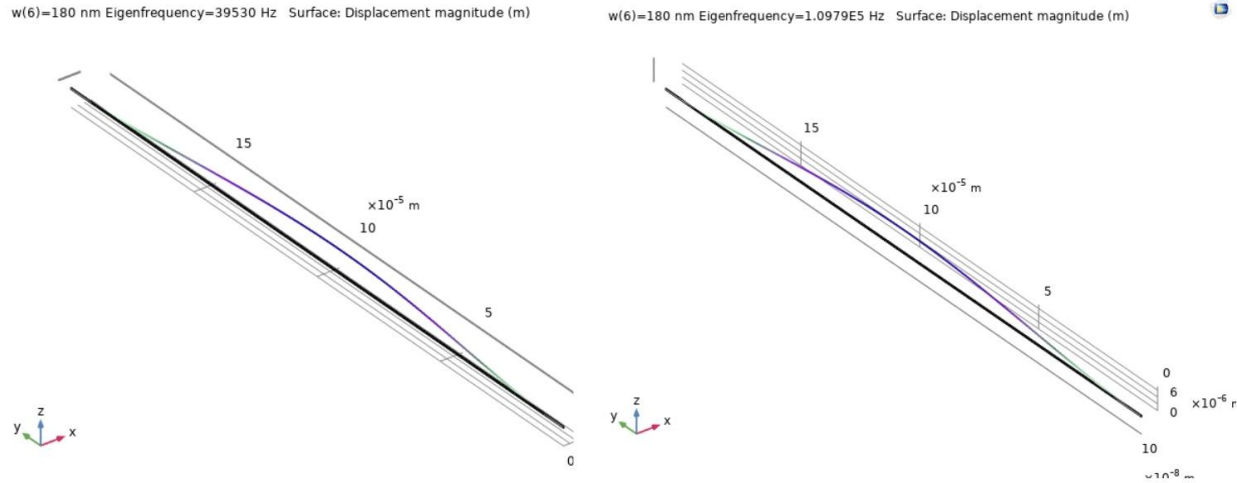


*Figure 38: Waveguide mode shapes for two different eigenfrequencies. Oscillations in the x direction (left) and y direction (right) were observed.*

In addition to computing eigenfrequencies, COMSOL also generates the mode shape associated with each eigenfrequency. We observed mode shapes where the waveguide was vertically displaced and horizontally displaced. Horizontal displacement of the waveguides would be problematic for the design because they would collide with the microdisk. We concluded that this would not be an issue because the mechanical actuator beneath the chip will only apply forces in the vertical direction. Furthermore, we will not be driving vibrations near the eigenfrequencies of the waveguides so it is very unlikely that these mode shapes will be resolved.

## Appendix I: Lumerical Coupling Simulations

The purpose of these simulations was to determine where to place the microdisk relative to the waveguide to ensure the most sensitive displacement measurements. A sensitive measurement requires large changes in transmission for small changes in displacement. The coupling gap is defined as the distance that separates the edge of the microdisk to the edge of the waveguide that passes by tangentially when the relative vertical distance between the two components is zero. We also looked at how coupling changes as the disk moves up and down relative to the waveguide.

We were investigating how light travels from medium to another which requires solving Maxwell's equations. Since the geometry of our system is not simple we used Lumerical, a simulation tool that uses the finite difference time domain method to solve Maxwell's equations numerically. See "[Finite-Difference Time-Domain Method](#)" on Wikipedia for more information.

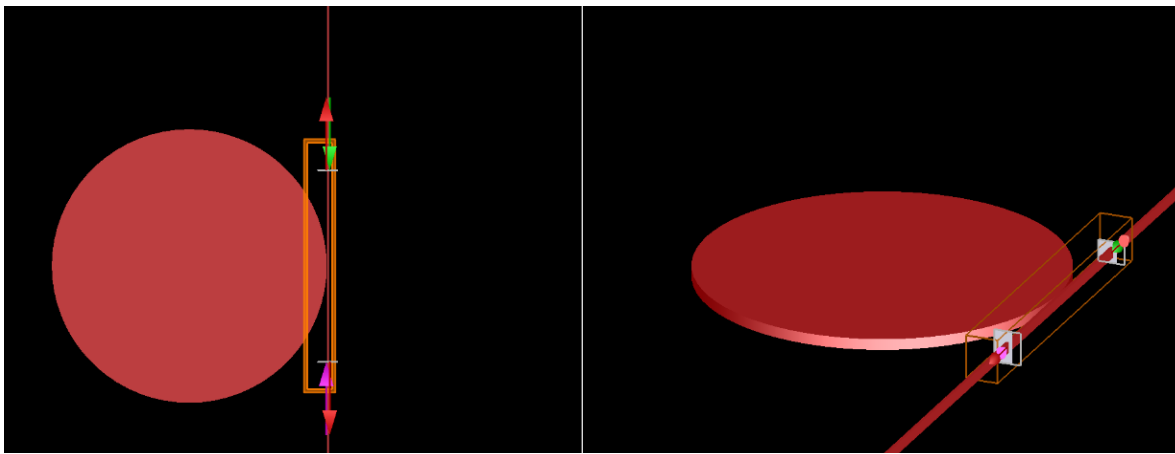
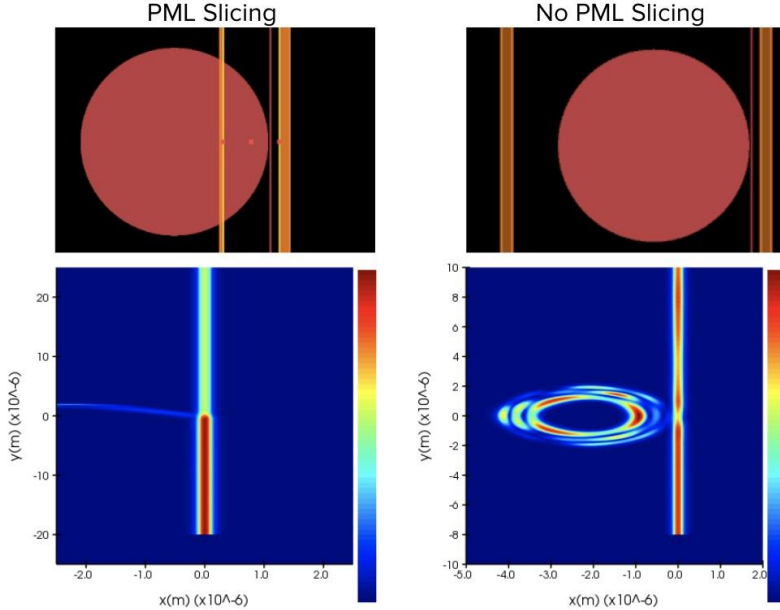


*Figure 39: Lumerical model to simulate coupling between a silicon microdisk and a silicon waveguide. The orange box defines the simulation region and input (pink) and output (green) ports inject and monitor light in the simulation.*

The model for this simulation consists of a microdisk disk, a waveguide, two ports and the simulation region. The waveguide and the disk are made of silicon and have a refractive index of 3.48. The waveguide is centred at the origin of the simulation and extends in the y direction and the disk is placed so that the faces are parallel to the XY plane. The disk and waveguide are both 500 nm thick, the disk radius and waveguide width was varied during the simulations and the waveguide's length was defined by the simulation region. The cutouts in our microdisk designs were not implemented in the model because light coupled into concave/circular objects primarily travel around the edge and circumference of the disk so the cutouts would not have significantly impacted the simulation.

In Lumerical, ports are objects that act as a light source and a light monitor. The input and output ports are placed along the waveguide at +70% and -70% of the disk radius from the origin to ensure that they do not interfere with the coupling between the disk and the waveguide. The mode and wavelength of the light injected into the waveguide are defined in the port and global light source settings.

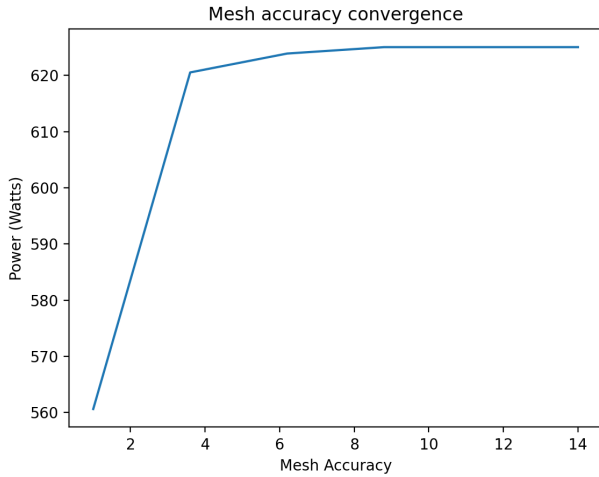
The simulation region is defined by the PML. It acts as an absorbing layer for wave equations to truncate the computation of simulations with infinite boundaries. Our initial instinct was to set up the PML to enclose the entire microdisk and waveguide. Ultimately we implemented a model where the PML sliced through the microdisk and only enclosed the portion directly adjacent to the waveguide.



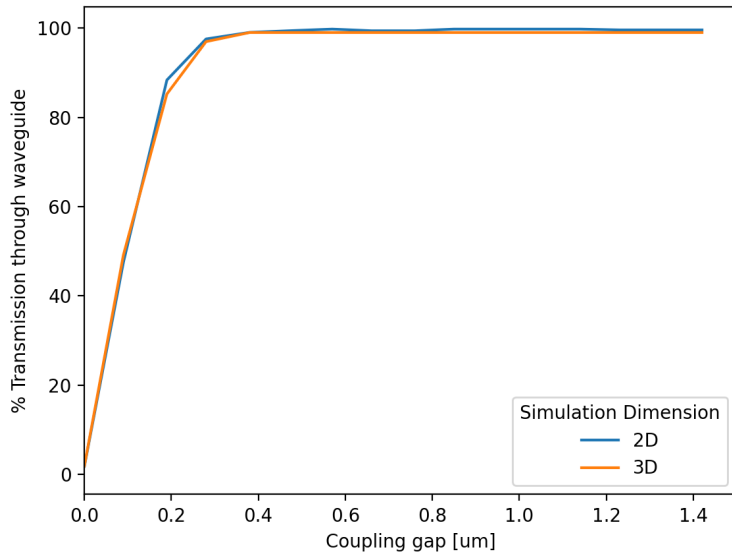
*Figure 40: The top 2 pictures show the difference in model set up when the PML is set to slice the microdisk (left) and enclose the microdisk (right). The bottom two pictures show the difference in behaviour of light for the two models. On the left, with PML slicing, the light from the waveguide is coupled into the disk and absorbed by the PML. On the right, without PML slicing, the light couples into the microdisk and some of it couples back into the waveguide.*

Figure 40 highlights the behaviour of light with the reduced simulation region and the full simulation region. With PML slicing any light that is coupled into the microdisk will be absorbed by the PML and without PML slicing, light that couples into the microdisk can couple back into the waveguide. This bi-directional coupling effect arises due to radiative bending losses in the microdisk. The effect becomes negligible for larger disk radii because bending losses decrease as radius increases (Musa, 2004). Since we are concerned primarily with coupling for 500  $\mu\text{m}$  microdisks, it was suitable to run the simulations with PML slicing.

In FDTD simulations, the mesh discretizes the simulation domain for solving Maxwell's equations. Increasing the number of mesh elements increases the accuracy of the simulation but also increases the time of the simulation. Based on the results in Figure 41, a mesh accuracy of 5 was used in the coupling gap simulations.



*Figure 41: A parameter sweep that measured the power of light through a port monitor as the mesh accuracy of the simulation was increased. The power measurement converged at a mesh accuracy of 5.*



*Figure 42: Plot of the transmission through a waveguide as a function of the coupling gap between a 2  $\mu\text{m}$  microdisk and a waveguide. The simulation was run once using a 2D simulation region (single plane only) and a 3D simulation region. Because the disk and waveguide are the same height the results were similar for both cases.*

In Lumerical the FDTD simulation space can be defined for a 2D or 3D region. Similarly to the mesh accuracy, a 3D simulation will take significantly longer but be more accurate than the 2D simulation. Figure 42 displays the results of a coupling gap simulation between a 2  $\mu\text{m}$  radius disk and waveguide for both a 2D and 3D simulation. The results were consistent between the two simulations so we used a 2D simulation region for all horizontal coupling gap simulations.

For vertical displacement simulations where the disk and waveguide do not remain in the same plane a 3D simulation region was used.

In FDTD simulations the solver is time-stepped. We found that the default simulation time of 1000 fs was suitable for smaller simulations when the disk radius was smaller than 50  $\mu\text{m}$ . However, as we scaled up the size of the microdisks we also had to increase the distance between the input and output ports. We observed that the light from the source did not reach the output port before the simulation ended. We found that at least a 20000 fs simulation time was required for a 500  $\mu\text{m}$  radius microdisk. This increased the time it took to complete each simulation considerably.

### Light waves/modes

In optics, modes describe the behaviour of light such as propagation, emission and absorption (Daendliker, 2000). Transverse modes of light refer to a radiation pattern of the electromagnetic field that is perpendicular to the field's direction of propagation. They arise due to boundary conditions imposed on waveguides and can be identified by solving Maxwell's equations with the given boundary conditions. Transverse electric (TE) modes have no electric field in the direction of propagation and transverse magnetic (TM) modes have no magnetic field in the direction of propagation.

The wavelength of light and transverse mode of light from the light source can be selected in the input port and global settings. We considered the effect of using TE or TM transverse modes and different wavelengths of light.

For the actual measurement setup we expect to use a laser light source with 1550 nm wavelength which is commonly used in optical experiments because it yields the lowest loss and attenuation of light through silicon waveguides (Robertson, 2018).

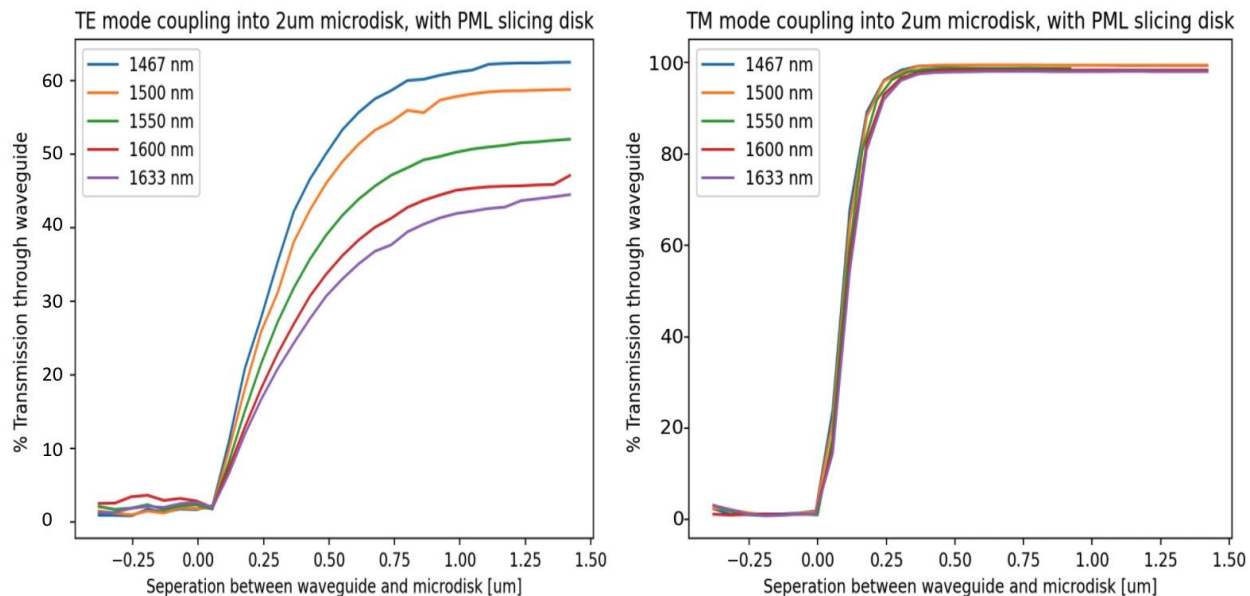


*Figure 43: Plots of the transmission through a waveguide as a function of coupling gap for a 2  $\mu\text{m}$  disk with TE (left) and TM (right) mode light sources. The transmission profile changes*

*considerably when the wavelength of the light source changes for TE modes while it remains relatively invariant for TM modes.*

The transmission of light through the waveguide as a function of the coupling gap between the waveguide and a 2  $\mu\text{m}$  radius disk for wavelengths from 1467 nm to 1633 nm are plotted in Figure 43. With TE modes, we saw that the transmission through the waveguide was dependent on the source's wavelength. Furthermore, the maximum transmission of light was only 60% demonstrating that with TE modes there is considerable attenuation through the waveguide. Conversely, with TM modes the amount of coupling was independent of wavelength. This is ideal because it demonstrates that our proposed measurement mechanism will still work if the light source needs to be changed due to set up limitations.

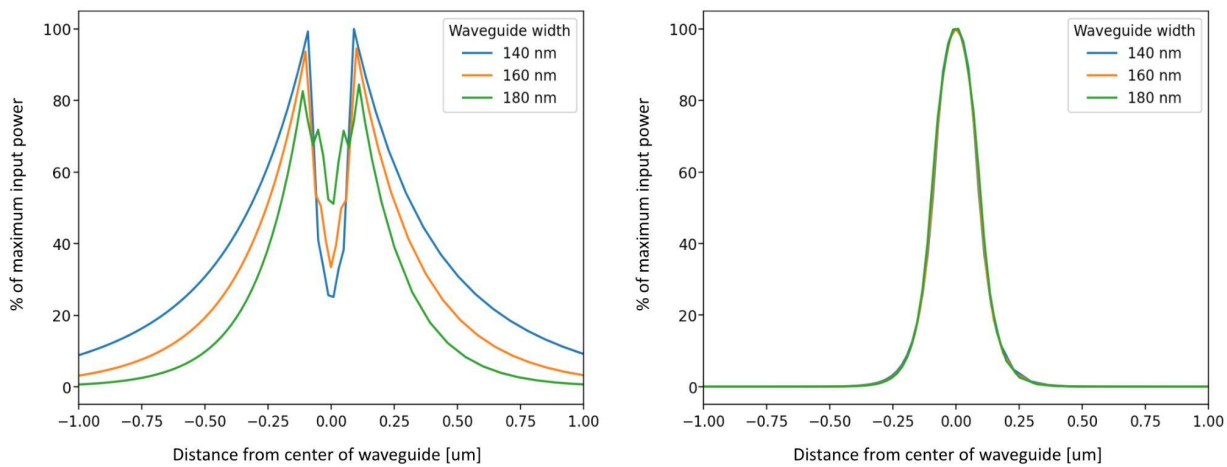


*Figure 44: Plots of relative light power as a function of distance from the centre of the waveguide measured for different waveguide widths. The right graph demonstrates the power profiles vary with waveguide width for TE modes and the left graph demonstrates that this is not a concern for TM modes.*

The power profiles in Figure 44 plots the power (as a percentage of the maximum input power) of the light source as a function of distance from the centre of the waveguide where the source was placed. We varied the width of the waveguide to see if that parameter affected the profile. Again, for TM modes the profile did not change with different waveguide dimensions whereas TE modes did.

We found that the decay in power for TM modes is larger than TE modes for the same change in distance. This is preferable because the amplitudes of oscillations we are trying to measure are on the nanometer scale so for small changes in position we will measure larger changes in transmission. Also, between 20% and 80% transmission the power profile is approximately linear. This behaviour will simplify the process for extracting ringdown time. For the following simulations we used a 1550 nm TM mode light source.

In Lumerical we set up two parametric sweeps. The first to identify the optimal coupling gap between the waveguide and microdisk when they are in the same plane and the second to understand the change in transmission as the microdisk is displaced vertically.

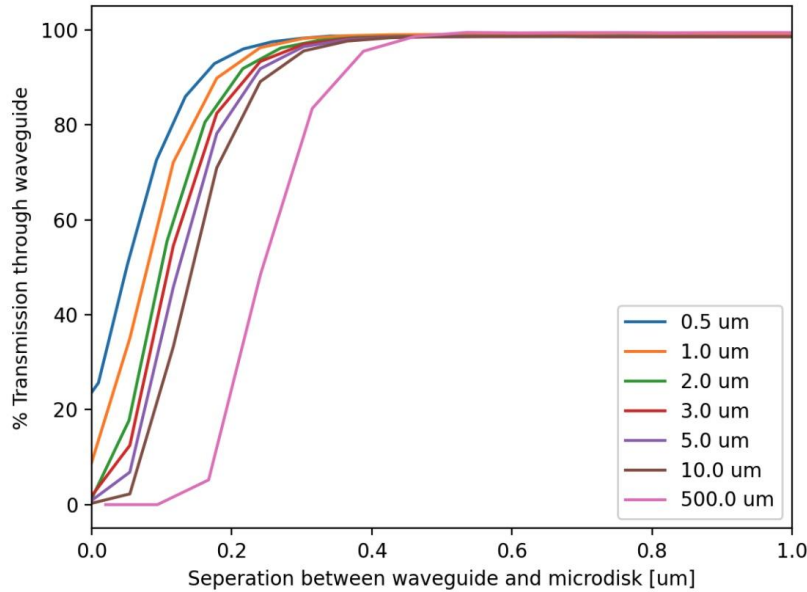


*Figure 45: Plot of the transmission of light through the waveguide as a function of the coupling gap between disks of varying radii and the waveguide. For larger disks, coupling begins and critical coupling is achieved at larger coupling gaps.*

For the coupling gap sweeps we started with smaller disks ( $0.5 \mu\text{m}$  -  $10 \mu\text{m}$  radius) to keep low simulation times, once we gained an understanding of the disks we scaled up to a  $500 \mu\text{m}$  radius disk. In the sweeps the position of the waveguide was fixed and the position of the disk was varied. Coupling of light from the waveguide into the disk begins when the % transmission through the waveguide drops from zero. We see that as the disk radius increases the initial coupling point is further away from the waveguide, this is because for the larger disks a longer portion of the waveguide will pass near the disk.

*Table 7: Calculated slopes of transmission vs coupling graphs for various disk radii.*

Radius [um]	Slope [ %/nm]
0.5	0.378
1	0.347
2	0.384
3	0.347
5	0.354

10	0.357
500	0.340

Measuring the slope of the linear region (20% - 80% transmission) of each curve in Figure 45, we found that the change in transmission for each nm change in coupling gap stays relatively constant for all disk sizes. This behaviour is ideal if the microdisk designs are altered in the future, for example if 500  $\mu\text{m}$  disks cannot be repeatedly fabricated without breaking.

Next we used a 3D simulation region to perform height sweeps where the vertical position of the microdisk was varied. We used a 10  $\mu\text{m}$  disk for these simulations rather than a 500  $\mu\text{m}$  disk because running the simulation for the 500  $\mu\text{m}$  disk at one height took over 12 hours. Although the exact values will not be the same we expect to observe the same trends for different disk sizes so this was a suitable starting point for the simulations.

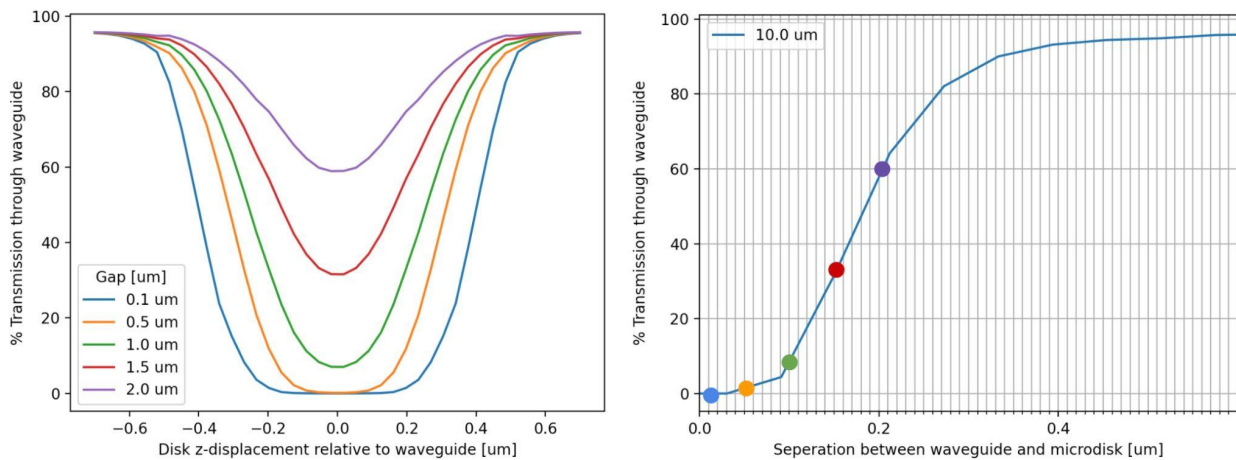


*Figure 46: Plot of the transmission of light through the waveguide as a function of vertical displacement between the waveguide and a 10  $\mu\text{m}$  microdisk for several fixed coupling gaps (left). The specific gaps are indicated on the 10  $\mu\text{m}$  coupling gap plot (right). Smaller coupling gaps have steeper transmission curves but a large region of 0 change in transmission.*

We repeated the height sweeps for several different coupling gaps as plotted in Figure 46 (left) and indicated in Figure 46 (right). The results demonstrate that as the coupling gap between the disk and the waveguide increases the change in transmission gets smaller for the same vertical displacement and the minimum transmission increases. This means for the chip design we want to place the microdisk and waveguide as close as possible to maintain the maximum transmission range and slope. Another key finding is that near 0 displacement, the slope of the transmission curve is zero. Because the waveguide and disk are the same thickness and particularly at small coupling gaps there needs to be a large offset to measure a change in transmission. This is problematic since currently the displacements of the microdisks are only several picometers large. We can work around this issue by fabricating the microdisk at a vertical offset to the waveguide so that any oscillations will immediately yield changes in transmission.

## Appendix J: Instrument specifications

Equipment	Specification
HP81689A Tunable Laser	<ul style="list-style-type: none"><li>• Line width = 20 MHz</li><li>• Min output power: -3 dBm (converts to 0.5 mW)</li><li>• "Output power (continuous power on during tuning): &gt;= 6 dBm"<ul style="list-style-type: none"><li>◦ Converts to approximately 4 mW</li></ul></li></ul>
 A photograph of the HP81689A tunable laser. It is a benchtop instrument with a digital display and several control knobs. A blue fiber optic cable is connected to its rear panel.	
Lucent X-2623Y Intensity Modulator	<ul style="list-style-type: none"><li>• Maximum RF voltage @ RF input: +/- 5V</li><li>• Maximum DC voltage @ RF input: +/- 20 V</li><li>• Maximum optical input power: 30 mW<ul style="list-style-type: none"><li>◦ <a href="https://www.rapidtables.com/convert/power/mW_to_dBm.html">https://www.rapidtables.com/convert/power/mW_to_dBm.html</a></li><li>◦ Converts to 14.77 dBm</li></ul></li><li>• The operating point seems to slightly drift for some time when the instruments are just starting up.</li><li>• Based on a lithium niobate crystal</li></ul>
 A photograph of two Lucent X-2623Y intensity modulators. They are rectangular metal enclosures with various ports and labels like "Lucent Electro-Optic Device" and "X-2623Y".	
Thorlabs DET01CFC Photodetector	<ul style="list-style-type: none"><li>• Can accept a peak power of 18 mW</li><li>• Saturation power of 5.5 mW at 1550 nm</li></ul>
 A photograph of a Thorlabs DET01CFC photodetector module. It is a small black rectangular device with a gold-colored connector and a label that reads "Thorlabs DET01CFC Model: LD500".	

## Appendix K: Power spectral density is a measure of system noise

In the following discussion, let's consider the case of measuring a voltage time series.

Noise spectral densities are often specified as amplitude spectral densities (ASD), or power spectral densities (PSD). If the random process is a voltage time series, its ASD has units Volt per square root Hz, and its PSD has units of volt squared per Hz.

Let  $n(t)$  be the noise we want to measure. Using a lock-in amplifier, we can measure the noise component at any specific frequency. By sweeping the frequency of the oscillator, we can in principle estimate the entire noise spectrum.

We model the noise at a specific frequency by

$$n_\omega(t) = \sqrt{2}R \sin(\omega t + \theta)$$

where  $\theta$  and  $R$  are random variables.

Through demodulation, the lock-in obtains the in-phase and quadrature components of the signal. Let  $X$  and  $Y$  be RMS amplitudes of the in-phase, and out-of-phase components, respectively.  $X$ ,  $Y$ ,  $R$  are related by

$$X = R \cos(\theta)$$

$$Y = R \sin(\theta)$$

So we can also express  $n_{\text{omega}}(t)$  by

$$n_\omega(t) = \sqrt{2}X \sin(\omega t) + \sqrt{2}Y \cos(\omega t)$$

For simplicity, we will consider  $X$ ,  $Y$  to be independent random variables that are normally distributed with a zero mean.

We can define the instantaneous noise power at a frequency  $\omega$  to be

$$\begin{aligned} p_\omega(t) &= n_\omega^2(t) = 2R \sin^2(\omega t + \theta) \\ &= 2X^2 \sin^2(\omega t) + 2Y^2 \cos^2(\omega t) + 2XY \sin(2\omega t) \end{aligned}$$

We can then define its time average:

$$P_\omega = \frac{1}{T} \int_T p_\omega(t) dt$$

By recalling that the time average sine or cosine squared is  $\frac{1}{2}$ , and that the time average  $\sin(2\omega t)$  is 0, we find that

$$P_\omega = R^2 = X^2 + Y^2$$

We see that the time averaged noise power is also a random variable. To get an estimate of "expected" amount of noise at some frequency, we consider the expectation value

$$\begin{aligned} P_n &= \mathbb{E}(P_\omega) = \mathbb{E}(R^2) \\ &= \mathbb{E}(X^2) + \mathbb{E}(Y^2) \end{aligned}$$

By definition of variance, we have

$$\text{Var}(X) = \mathbb{E}(X^2) - (\mathbb{E}(X))^2$$

Further, with the assumption that the  $\mathbf{X}$  and  $\mathbf{Y}$  have zero mean, we arrive at

$$\begin{aligned} P_n &= \mu_R^2 + \sigma_R^2 \\ &= \sigma_X^2 + \sigma_Y^2 \end{aligned}$$

With this background, we arrive at the interpretation of the noise spectral density,  $S_n$ , at some particular frequency:

$$S_n = \frac{P_n}{W}$$

where  $W$  is the measurement bandwidth. For a even more detailed discussion of different distributions of noise, please refer to (Alem, 2017)

## Appendix L: Amplitude demodulation using lock-in amplifier

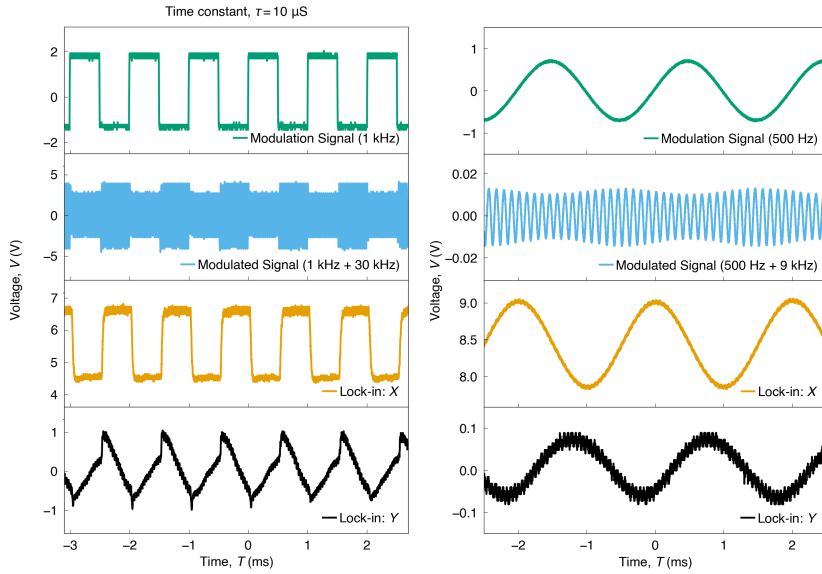


*Figure 47: Demonstration of real time envelope demodulation obtained via the set up shown in Figure 17. The demodulated signal closely resembled the modulation signal.*

For greater detail, please refer to (Zurich Instruments, 2016).

There are two main parameters to tune when setting up a lock-in amplifier. Our goal here is to give some intuition in how to tune the lock-in parameters.

1. Time constant
  - a. Determines the speed of lock-in measurements. A time constant too small will introduce unwanted measurement noise - the lock-in responds too quickly to changes in the signal. A time constant too large screens out any rapidly varying features
  - b. We found the following rule of thumb to determine the time constant. Begin by monitoring the lock-in outputs on an oscilloscope. Set the time constant to be roughly equal to the signal period. Increase the time constant in small increments until the desired output is found
2. Input filter order
  - a. The input filter order determines how fast the filter “cuts off” in the frequency domain
  - b. Both the time constant and the filter order contribute to the bandwidth of the filter in the frequency domain
  - c. A higher filter order slows down the measurement but lowers the noise in the measured signal

Other useful features include the “auto gain” and “auto reserve” buttons, which intelligently adjusts the output gain and dynamic reserve of the lock-in based on the signal input.

## Appendix M: Library of literature resources:

Paper	Topic	Comment
<a href="#">Ultralow-dissipation optomechanical resonators on a chip</a>	Microdisk Geometry	(paper, see highlighted sections)
<a href="#">Precision Ultrasound Sensing on a Chip</a>	Microdisk Geometry	(paper, see highlighted sections)
<a href="#">High-Q silicon optomechanical microdisk resonators at GHz frequencies</a>	Microdisk Geometry	(paper, see highlighted sections)
<a href="#">Cantilever Array-based artificial nose</a>	High Throughput	
<a href="#">Systemic Engineering of Waveguide-Resonator Coupling for Silicon Microring/microdisk/racetrack Resonators: theory &amp; experiment</a>	Integrated Waveguides	(see highlighted sections)
<a href="#">Photonic microdisk resonators in aluminum nitride</a>	Integrated Waveguides	(paper, see highlighted sections – note that the materials used are different from what we will use but the description of the coupling is still relevant)
<a href="#">Nanomechanical Motion Transducers for Miniaturized Mechanical Systems</a>		(section 3)
<a href="#">Using Higher Flexure Modes in non-contact force microscopy</a>	Free Space	(paper, see highlighted sections)
<a href="#">Thermal Noise in Interferometric Gravitational Wave</a>	Thermal Noise	
<a href="#">Investigation of Thermal Noise in Thin Silicon Structures</a>	Free Space	(paper, see sections 5-Experimental Setup and 7-Measurement Techniques in particular)
<a href="#">A technique for continuous measurement of the quality factor of mechanical oscillations</a>	Free Space	(Related to the continuous measurement method mentioned in "investigation of thermal noise in thin silicon structures")
<a href="#">Thorlabs: Quadrant Photodiode</a>	Free Space	(example of a quadrant photodiode – scroll to 'tech' tab for information on how they work)

<a href="#">Optomechanics with Whispering-Gallery Mode Optical Micro-Resonators</a>	Microdisk Geometry	
<a href="#">Theory of thermal noise in optical mirrors</a>		
<a href="#">Coating thermal noise</a>		
<a href="#">Progress in the measurement and reduction of thermal noise in optical coatings for gravitational-wave detectors</a>	Free Space	
<a href="#">Measurements of mechanical thermal noise and energy dissipation in optical dielectric coatings</a>	Free Space	Referred to in <b>Progress in the measurement and reduction of thermal noise in optical coatings for gravitational-wave detectors</b>
<a href="#">Cavity Optomechanics with silicon toroid microresonators down to low phonon occupancy</a>		
<a href="#">How to inspect your mesh - COMSOL</a>	Simulations	
<a href="#">Sensitive micromechanical displacement detection by scattering evanescent optical waves</a>		
<a href="#">Detection of nanomechanical motion by evanescent light wave coupling</a>		
<a href="#">Broadband all-photonic transduction of nanocantilevers</a>		
<a href="#">Remote displacement measurement using a passive interferometer with a fiber-optic link</a>		
<a href="#">Theoretical Analysis of Mechanical Displacement Measurement Using a Multiple Cavity Mode Transducer</a>		
<a href="#">Cavity-ringdown-spectroscopy-based study of high Q resonators in adddrop configuration</a>		
<a href="#">High resolution displacement measurements using waveguides</a>		
<a href="#">Design criteria of an integrated optics microdisplacement sensor</a>		
<a href="#">Evanescent field absorption in a passive optical fiber resonator using continuous-wave cavity ring-down spectroscopy</a>		
<a href="#">Optical fiber cavity ringdown for refractive index</a>		
<a href="#">Integrated nano-optomechanical displacement sensor with ultrawide optical bandwidth</a>		
<a href="#">Integrated_Optomechanical_Displacement_Sensor_B</a>		

<a href="#"><u>ased on a Photonic Crystal Cavity</u></a>		
<a href="#"><u>Optomechanical sensing with on-chip microcavities</u></a>		